Inorganic Chemistry

Heterometallic Integer-Spin Analogues of $S = \frac{9}{2}$ Mn$_4$ Cubane Single-Molecule Magnets

Patrick L. Feng,[†] Christopher C. Beedle,[†] Changhyun Koo,[‡] Wolfgang Wernsdorfer,[§] Motohiro Nakano,[||] Stephen Hill,[‡] and David N. Hendrickson[*,†]

Department of Chemistry and Biochemistry, University of California, San Diego, La Jolla, California 92093-0358, Institut Néel, CNRS, BP166, Grenoble Cedex 9, France, Department of Physics, University of Florida, Gainesville, Florida 32611, and Division of Applied Chemistry, Osaka University, Suita, Osaka 565-0871, Japan

A family of distorted heterometallic cubanes, [Mn$^{III}_3$Ni^{II}(hmp)$_3$O(N$_3$)$_3$(O$_2$CR)$_3$], where O$_2$CR$^-$ is benzoate (**1**), 3-phenylpropionate (**2**), 1-adamantanecarboxylate (**3**), or acetate (**4**) and hmp$^-$ is the anion of 2-pyridinemethanol, was synthesized and structurally as well as magnetically characterized. These complexes have a distorted-cubane core structure similar to that found in the $S = \frac{9}{2}$ Mn$_4$ cubane family of complexes. Complexes **1**, **3**, and **4** crystallize in rhombohedral, hexagonal, and cubic space groups, respectively, and have C_3 molecular symmetry, while complex **2** crystallizes in the monoclinic space group Cc with local C_1 symmetry. Magnetic susceptibility and magnetization hysteresis measurements and high-frequency electron paramagnetic resonance (HFEPR) spectroscopy established that complexes **1**−**4** have $S = 5$ spin ground states with axial zero-field splitting (ZFS) parameters (D) ranging from −0.20 to −0.33 cm^{-1}. Magnetization versus direct-current field sweeps below 1.1 K revealed hysteresis loops with magnetization relaxation, definitely indicating that complexes **1**−**4** are single-molecule magnets that exhibit quantum tunneling of magnetization (QTM) through an anisotropy barrier. Complex **2** exhibits the smallest coercive field and fastest magnetization tunneling rate, suggesting a significant rhombic ZFS parameter (E), as expected from the low C_1 symmetry. This was confirmed by HFEPR spectroscopy studies on single crystals that gave the following parameter values for complex **2**: $g_z = 1.98$, $g_x = g_y = 1.95$, $D = -0.17$ cm^{-1}, $B_4^0 = -6.68 \times 10^{-5}$ cm^{-1}, $E = 6.68 \times 10^{-3}$ cm^{-1}, and $B_4^2 = -1.00 \times 10^{-4}$ cm^{-1}. Single-crystal HFEPR data for complex **1** gave $g_z = 2.02$, $g_x = g_y = 1.95$, $D = -0.23$ cm^{-1}, and $B_4^0 = -5.68 \times 10^{-5}$ cm^{-1}, in keeping with the C_3 site symmetry of this Mn$_3$Ni complex. The combined results highlight the importance of spin-parity effects and molecular symmetry, which determine the QTM rates.

Introduction

The discovery of a tetranuclear mixed-valence manganese complex at the active site of the oxygen-evolving center in photosystem II generated intense interest in the synthesis of model complexes that would exhibit similar structural and spectroscopic properties and led to the serendipitous preparation of high-valence Mn$_4$ cubane complexes.[1−10] These

complexes gained additional significance with the discovery of single-molecule magnets (SMMs), as numerous examples exhibited such behavior.[5,11] SMMs are individual molecules that possess a significant barrier to magnetization reversal as a result of a large ground-state spin value (S) and

* To whom correspondence should be addressed. E-mail: dhendrickson@ucsd.edu.
† University of California, San Diego.
‡ University of Florida.
§ Institut Néel.
|| Osaka University.

(1) Aromi, G.; Wemple, M. W.; Aubin, S. J.; Folting, K.; Hendrickson, D. N.; Christou, G. *J. Am. Chem. Soc.* **1998**, *120*, 5850–5851.

(2) Aubin, S. M. J.; Dilley, N. R.; Pardi, L.; Krzystek, J.; Wemple, M. W.; Brunel, L. C.; Maple, M. B.; Christou, G.; Hendrickson, D. N. *J. Am. Chem. Soc.* **1998**, *120*, 4991–5004.

(3) Aubin, S. M. J.; Wemple, M. W.; Adams, D. M.; Tsai, H. L.; Christou, G.; Hendrickson, D. N. *J. Am. Chem. Soc.* **1996**, *118*, 7746–7754.

(4) Bashkin, J. S.; Chang, H. R.; Streib, W. E.; Huffman, J. C.; Hendrickson, D. N.; Christou, G. *J. Am. Chem. Soc.* **1987**, *109*, 6502–6504.

(5) Hendrickson, D. N.; Christou, G.; Schmitt, E. A.; Libby, E.; Bashkin, J. S.; Wang, S. Y.; Tsai, H. L.; Vincent, J. B.; Boyd, P. D. W.; Huffman, J. C.; Folting, K.; Li, Q. Y.; Streib, W. E. *J. Am. Chem. Soc.* **1992**, *114*, 2455–2471.

significant easy-axis (Ising) magnetic anisotropy.[12–14] This anisotropy is reflected by a negative value of the axial zero-field splitting (ZFS) parameter (D), resulting in theoretical barriers to magnetization reversal of DS^2 and $D(S^2 - \frac{1}{4})$ for integer and half-integer S values, respectively. A significant barrier leads to slow relaxation of the magnetization, resulting in frequency-dependent out-of-phase alternating-current (ac) magnetic susceptibility (χ''_M) signals and hysteresis loops in plots of magnetization versus applied direct-current (dc) field.

Two well-studied types of Mn₄ cubane SMMs include $[Mn_4O_3X(O_2CMe_3)_3(dbm)_3]$, where X^- is Cl^-, Br^-, N_3^-, NCO^-, OH^-, or MeO^- and dbm⁻ is the anion of dibenzoylmethane, and $[Mn_4O_3Cl_4(O_2CR)_3(py)_3]$, where R is Me or Et and py is pyridine.[5,11] The complexes in both series have well-isolated $S = \frac{9}{2}$ spin ground states and contain a distorted-cubane $[Mn_4(\mu_3\text{-}O)_3(\mu_3\text{-}X)]^{6+}$ mixed-valence core containing one Mn^{IV} and three Mn^{III} ions. The magnetic properties of these complexes exhibit interesting quantum phenomena such as spin-parity-dependent quantum tunneling of magnetization (QTM),[15] spin–spin cross relaxation,[16] and quantum coherence (QC).[17] The discovery of antiferromagnetically coupled dimers of two Mn^{IV}Mn₃^{III} complexes led to the observation of unique hysteresis loops in which the intermolecular exchange interaction results in a bias that shifts from zero field the magnetic field at which the quantum tunneling occurs.[18] The exchange bias within this [Mn₄]₂ dimer also made possible the study of QC of magnetization, for which the linewidths of high-frequency electron paramagnetic resonance (HFEPR) transitions allowed for estimated QC times on the order of 1 ns.[17] These findings have important implications for potential applications such as molecular memory devices, where a bit of information would be stored on a single molecule, and quantum information processing, where each molecule would function as a quantum bit.[17–19]

In the present work, we investigated the structural and magnetic properties of a new, related family of heterometallic cubanes. These complexes have well-isolated $S = 5$ spin ground states and contain one Ni^{II} and three Mn^{III} ions in a core structure similar to that in the $S = \frac{9}{2}$ Mn₄ cubanes. Important differences in their magnetic properties exist, particularly with respect to their spin Hamiltonian parameters, hysteresis loops, and QTM rates; these differences result from the integer-spin ground states and molecular symmetries of these complexes. The results of in-depth magnetization and HFEPR experiments are described, and the similarities and differences between the previously reported $S = \frac{9}{2}$ Mn₄ SMMs and our new $S = 5$ Mn₃Ni SMMs are highlighted.

Experimental Section

Materials and Synthesis. All of the starting materials were reagent grade and used as received. ***Caution!*** *NaN₃ is toxic and potentially explosive. Although no problems were encountered in this work, these materials should be handled with extreme care.*

$[Mn_3Ni(hmp)_3O(N_3)_3(C_7H_5O_2)_3]$·2CHCl₃ (1). Mn(C₇H₅O₂)₂· H₂O (0.376 g, 1.02 mmol) and NiCl₂·6H₂O (0.256 g, 1.08 mmol) were added to 40 mL of CHCl₃. NaN₃ (0.070 g, 1.08 mmol), 2-pyridinemethanol (hmpH) (0.22 mL, 2.28 mmol), and NBu₄MnO₄ (0.092 g, 0.255 mmol) were quickly added, and the mixture was stirred for 30 min. The red-brown solution was decanted from a sticky white precipitate and layered with Et₂O. Large, red-brown block crystals formed overnight in 75% yield (based on Mn). Anal. Calcd for C₄₁H₃₅Mn₃NiN₁₂O₁₀Cl₆ (**1**): C, 38.11; H, 2.73; N, 13.01. Found: C, 39.39; H, 3.19; N, 14.08.

$[Mn_3Ni(hmp)_3O(N_3)_3(C_9H_9O_2)_3]$ (2). Mn(NO₃)₂·4H₂O (0.280 g, 1.12 mmol) and Ni(NO₃)₂·6H₂O (0.170 g, 0.59 mmol) were added with stirring to 40 mL of a solution of NaN₃ (0.090 g, 1.38 mmol), 3-phenylpropionic acid (0.190 g, 1.27 mmol), and hmpH (0.22 mL, 2.28 mmol) in CHCl₃. n-NBu₄MnO₄ (0.092 g, 0.255 mmol) was added over 5 min, and the resulting mixture was stirred for 3 h. The dark-brown filtrate was then layered with isopropyl ether and left undisturbed for 1 week. Black, cube-shaped crystals were retrieved in 71% yield (based on Mn). Anal. Calcd for C₄₅H₄₅Mn₃NiN₁₂O₁₀ (**2**): C, 47.52; H, 3.99; N, 14.78. Found: C, 47.21; H, 3.87; N, 14.96.

$[Mn_3Ni(hmp)_3O(N_3)_3(C_{11}H_{15}O_2)_3]$·CH₂Cl₂ (3). Mn(NO₃)₂· 4H₂O (0.250 g, 1.00 mmol) and Ni(NO₃)₂·6H₂O (0.200 g, 0.70 mmol) were added with stirring to 50 mL of a solution of NaN₃ (0.070 g, 1.08 mmol), 1-adamantanecarboxylic acid (0.25 g, 1.39 mmol), and hmpH (0.22 mL, 2.28 mmol) in CH₂Cl₂. NBu₄MnO₄ (0.092 g, 0.255 mmol) was added over 5 min, and the resulting mixture was stirred for 30 min. The dark-red filtrate was then carefully layered with Et₂O. Long black needles (10 mm × 1 mm × 1 mm) were collected after 3 days in 82% yield (based on Mn). Anal. Calcd for C₅₂H₆₅Mn₃NiN₁₂O₁₀Cl₂ (**3**): C, 47.58; H, 4.99; N, 12.81. Found: C, 47.71; H, 4.99; N, 12.89.

$[Mn_3Ni(hmp)_3O(N_3)_3(C_2H_3O_2)_3]$ (4). Mn(OAc)₂·4H₂O (0.730 g, 2.98 mmol) and Ni(OAc)₂·4H₂O (0.354 g, 1.42 mmol) were added to 50 mL of CHCl₃. NaN₃ (0.200 g, 3.08 mmol) and hmpH (0.812 mL, 8.43 mmol) were slowly added, and the resulting mixture was stirred overnight. The resulting red-brown solution was filtered and carefully layered with Et₂O. Well-formed dark-red pyramidal crystals were obtained in 64% yield (based on Mn) after

(6) Vincent, J. B.; Christmas, C.; Chang, H. R.; Li, Q. Y.; Boyd, P. D. W.; Huffman, J. C.; Hendrickson, D. N.; Christou, G. *J. Am. Chem. Soc.* **1989**, *111*, 2086–2097.

(7) Vincent, J. B.; Christmas, C.; Huffman, J. C.; Christou, G.; Chang, H. R.; Hendrickson, D. N. *Chem. Commun.* **1987**, 236–238.

(8) Ferreira, K. N.; Iverson, T. M.; Maghlaoui, K.; Barber, J.; Iwata, S. *Science* **2004**, *303*, 1831–1838.

(9) Yachandra, V. K.; Derose, V. J.; Latimer, M. J.; Mukerji, I.; Sauer, K.; Klein, M. P. *Science* **1993**, *260*, 675–679.

(10) Yano, J.; Kern, J.; Sauer, K.; Latimer, M. J.; Pushkar, Y.; Biesiadka, J.; Loll, B.; Saenger, W.; Messinger, J.; Zouni, A.; Yachandra, V. K. *Science* **2006**, *314*, 821–825.

(11) Wang, S. Y.; Tsai, H. L.; Libby, E.; Folting, K.; Streib, W. E.; Hendrickson, D. N.; Christou, G. *Inorg. Chem.* **1996**, *35*, 7578–7589.

(12) Sessoli, R.; Tsai, H. L.; Schake, A. R.; Wang, S. Y.; Vincent, J. B.; Folting, K.; Gatteschi, D.; Christou, G.; Hendrickson, D. N. *J. Am. Chem. Soc.* **1993**, *115*, 1804–1816.

(13) Sessoli, R.; Gatteschi, D.; Caneschi, A.; Novak, M. A. *Nature* **1993**, *365*, 141–143.

(14) Christou, G.; Gatteschi, D.; Hendrickson, D. N.; Sessoli, R. *MRS Bull.* **2000**, *25*, 66–71.

(15) Wernsdorfer, W.; Bhaduri, S.; Boskovic, C.; Christou, G.; Hendrickson, D. N. *Phys. Rev. B* **2002**, *65*, 180403.

(16) Wernsdorfer, W.; Bhaduri, S.; Tiron, R.; Hendrickson, D. N.; Christou, G. *Phys. Rev. Lett.* **2002**, *89*, 197201.

(17) Hill, S.; Edwards, R. S.; Aliaga-Alcalde, N.; Christou, G. *Science* **2003**, *302*, 1015–1018.

(18) Wernsdorfer, W.; Allaga-Alcalde, N.; Hendrickson, D. N.; Christou, G. *Nature* **2002**, *416*, 406–409.

(19) Tejada, J.; Chudnovsky, E. M.; del Barco, E.; Hernandez, J. M.; Spiller, T. P. *Nanotechnology* **2001**, *12*, 181–186.

Table 1. Crystal Data and Structure Refinement Parameters for Compounds **1–4**

parameter	1	2	3	4
formula	$C_{41}H_{35}Mn_3NiN_{12}O_{10}Cl_6$	$C_{45}H_{45}Mn_3NiN_{12}O_{10}$	$C_{52}H_{65}Mn_3NiN_{12}O_{10}Cl_2$	$C_{24}H_{27}Mn_3NiN_{12}O_{10}$
formula weight	1292.02	1137.42	1312.56	867.05
crystal system	trigonal	monoclinic	hexagonal	cubic
space group	$R3c$ (No. 161)	Cc (No. 9)	$P6_3$ (No. 173)	$I\bar{4}3d$ (No. 220)
a (Å)	15.453(4)	25.724(2)	16.264(5)	23.469(6)
b (Å)	15.453(4)	15.9015(13)	16.264(5)	23.469(6)
c (Å)	38.060(10)	14.1776(11)	24.634(5)	23.469(6)
α (deg)	90.00	90.00	90.00	90.00
β (deg)	90.00	122.9980(10)	90.00	90.00
γ (deg)	120.00	90.00	120.00	90.00
V (Å^3)	7870(3)	4863.9(7)	5643(3)	12926(6)
Z	6	4	4	16
T (K)	100(2)	208(2)	208(2)	100(2)
μ (mm^{-1})	1.430	1.212	1.148	1.793
D (g cm^{-3})	1.636	1.553	1.543	1.782
F_{000}	3816	2328	2704	21024
no. of reflections measured	17761	16334	40546	14794
no. of reflections used	2870	7299	5038	1527
no. of parameters	196	640	487	152
R1[a]	0.0367	0.0411	0.0383	0.0320
wR2[b]	0.0394	0.0501	0.0488	0.0459
goodness of fit on F^2	1.090	0.983	1.028	0.842

[a] $R1 = \sum||F_o| - |F_c||/\sum|F_o|$ [using data with $I > 2.00\sigma(I)$]. [b] $wR2 = [\sum w(F_o^2 - F_c^2)^2/\sum w(F_o^2)^2]^{1/2}$ (all data).

3 weeks. Anal. Calcd for $C_{24}H_{27}Mn_3NiN_{12}O_{10}$ (**4**): C, 33.25; H, 3.14; N, 19.39. Found: C, 32.16; H, 3.23; N, 20.10.

Physical Measurements. Elemental analyses were performed by NuMega Resonance Laboratories (San Diego, CA) for complexes **1**−**4**. Direct-current magnetic susceptibility measurements employed finely ground polycrystalline samples of complexes **1**−**4** that were restrained in eicosane to prevent torquing of the microcrystallites in the externally applied magnetic field. The measurements were performed using a Quantum Design MPMS-5 magnetometer equipped with a 5.5 T magnet in the 1.8−300 K temperature range with applied fields of 0.1−50 kG. Alternating-current magnetic susceptibility measurements were obtained between 1 and 5 K with a 3 G ac field at frequencies in the range of 10−997 Hz with zero applied dc magnetic field using a Quantum Design MPMS-2 magnetometer. Data were corrected for diamagnetic contributions resulting from the sample rod, the capsule, and eicosane. Corrections for diamagnetism were estimated from Pascal's constants, yielding the overall paramagnetic contribution to the molar magnetic susceptibility. Single-crystal magnetization hysteresis and magnetic relaxation measurements at temperatures below 1.8 K were performed using a micro-SQUID array.[20] High-frequency (40−160 GHz) electron paramagnetic resonance measurements were carried out between 2 and 20 K on single crystals of complexes **1** and **2** using a millimeter-wave vector network analyzer (MVNA) and a sensitive cavity technique.[21] A split-pair superconducting magnet was used to apply a transverse dc magnetic field in the range from 0 to 7 T. The angle dependence of the HFEPR spectra for complexes **1** and **2** was investigated by using the stepper motor associated with a Quantum Design Physical Property Measurement System (PPMS) to rotate the sample in the applied dc magnetic field. The temperature was also controlled by the PPMS.

X-ray Crystallography. Diffraction intensity data were collected at −173 °C for complexes **1** and **4** and at −65 °C for complexes **2** and **3**. A Bruker Smart Apex CCD diffractometer was used, and the resulting data were integrated using the Bruker SAINT software program and corrected for absorption using the Bruker SADABS program. Crystal data, data collection, and refinement parameters for complexes **1**−**4** are given in Table 1.

The structures of complexes **1**−**4** were solved by direct methods (SHELXS-97), developed by successive difference Fourier syntheses, and refined by full-matrix least-squares on all F^2 data. All non-hydrogen atoms were refined anisotropically, and hydrogen atoms were placed in calculated positions with temperature factors fixed at 1.2 or 1.5 times the equivalent isotropic U values for the C atoms to which they were bonded. To account for unresolved solvent in complex **1**, the PLATON program SQUEEZE was used; it found 673 electrons per unit cell, or 2 molecules of chloroform (58 electrons per molecule) per molecular unit. Solvent electron density was therefore included in the molecular formula of **1** as $2CHCl_3$. The methylene chloride solvate molecule in complex **3** is threefold disordered, resulting in a chlorine occupancy of $^2/_3$ in each of the three sites. The occupancies were determined through refinement using the FVAR command in SHELXS-97.

Results and Discussion

Synthesis. In certain cases it has been possible to obtain some synthetic control over the formation of polynuclear transition-metal complexes that function as SMMs by selectively modifying the periphery of preformed structural types, as has been shown through carboxylate replacement in the well-studied family of $[Mn_{12}O_{12}(O_2CR)_{16}(H_2O)_4]$ complexes.[12,22–26] These ligand substitution studies have been instrumental in developing an understanding of the

(20) Wernsdorfer, W. *Adv. Chem. Phys.* **2001**, *118*, 99–190.

(21) Mola, M.; Hill, S.; Goy, P.; Gross, M. *Rev. Sci. Instrum.* **2000**, *71*, 186–200.

(22) Artus, P.; Boskovic, C.; Yoo, J.; Streib, W. E.; Brunel, L. C.; Hendrickson, D. N.; Christou, G. *Inorg. Chem.* **2001**, *40*, 4199–4210.

(23) Aubin, S. M. J.; Spagna, S.; Eppley, H. J.; Sager, R. E.; Christou, G.; Hendrickson, D. N. *Chem. Commun.* **1998**, 803–804.

(24) Eppley, H. J.; Tsai, H. L.; de Vries, N.; Folting, K.; Christou, C.; Hendrickson, D. N. *J. Am. Chem. Soc.* **1995**, *117*, 301–317.

(25) Chakov, N. E.; Abboud, K. A.; Zakharov, L. N.; Rheingold, A. L.; Hendrickson, D. N.; Christou, G. *Polyhedron* **2003**, *22*, 1759–1763.

(26) Boskovic, C.; Brechin, E. K.; Streib, W. E.; Folting, K.; Bollinger, J. C.; Hendrickson, D. N.; Christou, G. *J. Am. Chem. Soc.* **2002**, *124*, 3725–3736.

nature of magnetization relaxation in these complexes, particularly with respect to intermolecular interactions and coupling to the environment.[27–29]

In view of the synthetic insight gained through these and similar studies, we decided to investigate heterometallic reactions involving 2-pyridinemethanol and sodium azide. This approach was chosen for many reasons. First, heterometallic complexes should provide the opportunity for tuning the spin of the ground state, the magnetic exchange interactions, and the anisotropy relative to those in homometallic examples.[30,31] This has previously been seen in $[Mn_{11}\text{-}CrO_{12}(O_2CCH_3)_{16}(H_2O)_4]$, where a Cr^{III} ion occupies the place of a Mn^{III} ion in the parent $[Mn_{12}O_{12}(O_2CCH_3)_{16}(H_2O)_4]$ complex.[31] This modification resulted in a change of the spin ground state from $S = 10$ to $S = {}^{19}/_2$ and the observation of phenomena such as dipolar-biased QTM.[31]

The ligand 2-pyridinemethanol was chosen because of its versatility as a bridging ligand in polynuclear complexes.[32–36] The azide anion was chosen because it has been shown to facilitate ferromagnetic exchange interactions when bridging transition-metal ions in the commonly seen end-on ($\mu_{1,1}$) bridging mode.[37] This could give SMMs with higher blocking temperatures, since the height of the barrier for magnetization reversal is affected by changes to the spin ground state. Although the azido ligands in complexes **1**−**4** do not ferromagnetically couple magnetic centers as initially hoped, they are a required component for the synthesis of these new complexes. As a result, our goal of synthesizing heterometallic examples of a known polynuclear SMM was accomplished.

Description of the Structures of 1−4. The molecular structures of complexes **1** and **2** are shown in Figures 1 and 2, respectively, while those for complexes **3** and **4** are given in Figures S1 and S2, respectively, in the Supporting Information. Crystallographic data for all four complexes are provided in Table 1. A simplified view of the core structure of complexes **1**, **3**, and **4** is given in Figure 3, and a similar view of complex **2** is displayed in Figure 4. Selected bond
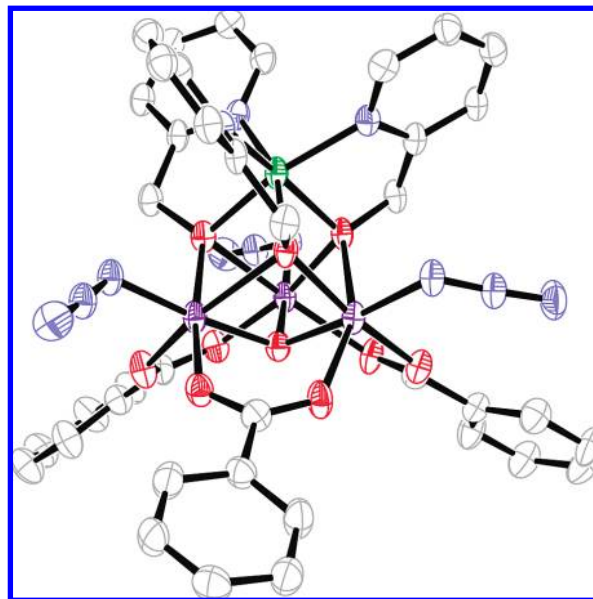

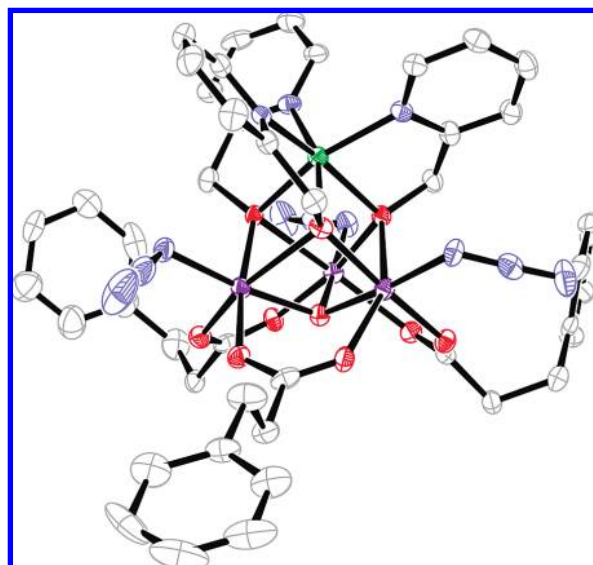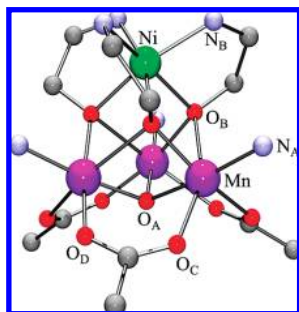**Figure 1.** ORTEP of complex **1**. Ellipsoids are shown at 50% probability.

Figure 2. ORTEP of complex **2**. Ellipsoids are shown at 50% probability.

distances and angles for complexes **1**, **3**, and **4** are summarized in Table 2 and those for complex **2** in Table 3.

Each compound possesses a $[Mn_3NiO_4]^{6+}$ cubane core structure that can be described as a Mn₃Ni trigonal pyramid having the Ni^{II} ion at the apex and a Mn^{III}_3 triangle at the base. The hexacoordinate Ni^{II} coordination environment is composed of three bidentate hmp⁻ ligands, each of whose alkoxo O atom bridges to a Mn^{III} ion. For all of the structures except **2**, the Mn^{III} ions are arranged in an equilateral triangle by virtue of their crystallographically imposed C_3 symmetry. A single μ_3-O^{2-} ion bridges the Mn^{III} ions and resides between 0.691 and 0.730 Å below the plane of the Mn^{III}_3 triangle. Each of the Mn^{III} ions is also coordinated by a terminal N_3^- ligand and two oxide ions, one from each of two bidentate carboxylate groups. The ligand arrangement for complexes **1**−**4** imparts a handedness to each molecule, allowing both Δ and Λ isomers to be identified. All of the

(27) Chakov, N. E.; Lee, S. C.; Harter, A. G.; Kuhns, P. L.; Reyes, A. P.; Hill, S. O.; Dalal, N. S.; Wernsdorfer, W.; Abboud, K. A.; Christou, G. *J. Am. Chem. Soc.* **2006**, *128*, 6975–6989.
(28) Aubin, S. M. J.; Sun, Z.; Eppley, H. J.; Rumberger, E. M.; Guzei, I. A.; Folting, K.; Gantzel, P. K.; Rheingold, A. L.; Christou, G.; Hendrickson, D. N. *Inorg. Chem.* **2001**, *40*, 2127–2146.
(29) Hill, S.; Anderson, N.; Wilson, A.; Takahashi, S.; Petukhov, K.; Chakov, N. E.; Murugesu, M.; North, J. M.; del Barco, E.; Kent, A. D.; Dalal, N. S.; Christou, G. *Polyhedron* **2005**, *24*, 2284–2292.
(30) Oshio, H.; Nihei, M.; Koizumi, S.; Shiga, T.; Nojiri, H.; Nakano, M.; Shirakawa, N.; Akatsu, M. *J. Am. Chem. Soc.* **2005**, *127*, 4568–4569.
(31) Hachisuka, H.; Awaga, K.; Yokoyama, T.; Kubo, T.; Goto, T.; Nojiri, H. *Phys. Rev. B* **2004**, *70*, 104427.
(32) Bolcar, M. A.; Aubin, S. M. J.; Folting, K.; Hendrickson, D. N.; Christou, G. *Chem. Commun.* **1997**, 1485–1486.
(33) Yoo, J.; Yamaguchi, A.; Nakano, M.; Krzystek, J.; Streib, W. E.; Brunel, L. C.; Ishimoto, H.; Christou, G.; Hendrickson, D. N. *Inorg. Chem.* **2001**, *40*, 4604–4616.
(34) Yang, E. C.; Hendrickson, D. N.; Wernsdorfer, W.; Nakano, M.; Zakharov, L. N.; Sommer, R. D.; Rheingold, A. L.; Ledezma-Gairaud, M.; Christou, G. *J. Appl. Phys.* **2002**, *91*, 7382–7384.
(35) Harden, N. C.; Bolcar, M. A.; Wernsdorfer, W.; Abboud, K. A.; Streib, W. E.; Christou, G. *Inorg. Chem.* **2003**, *42*, 7067–7076.
(36) Yang, E. C.; Wernsdorfer, W.; Hill, S.; Edwards, R. S.; Nakano, M.; Maccagnano, S.; Zakharov, L. N.; Rheingold, A. L.; Christou, G.; Hendrickson, D. N. *Polyhedron* **2003**, *22*, 1727–1733.
(37) Kahn, O. *Molecular Magnetism*; VCH: New York, 1993; pp xvi, 380.

Figure 3. Representation of the core bond connectivities in the C_3 complexes **1**, **3**, and **4**. Selected carbon and nitrogen atoms have been removed for clarity.
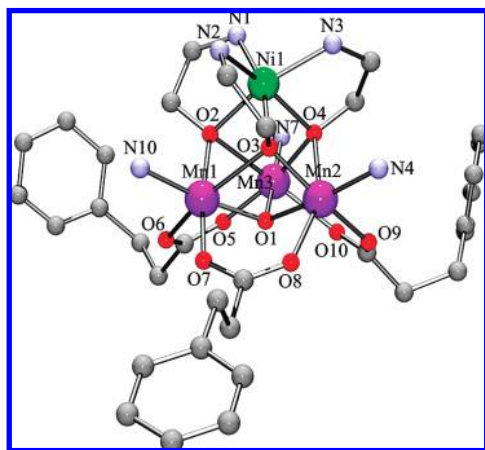
Figure 4. Representation of the core bond connectivities in the C_1 complex **2**. Selected carbon and nitrogen atoms have been omitted for clarity.

Table 2. Comparison of Selected Bond Distances (Å) and Angles (deg) for Complexes **1**, **3**, and **4**[a]

	1	**3**	**3***[b]	**4**
Mn–O$_A$	1.892	1.883	1.893	1.882
Mn–O$_B$ (JT)	2.375	2.248	2.295	2.298
Mn–O$_B$	1.966	2.023	1.983	1.956
Mn–O$_C$ (JT)	2.176	2.105	2.135	2.150
Mn–O$_D$	1.936	1.975	1.945	1.924
Mn–N$_A$	1.946	1.942	1.940	1.933
Ni–O$_B$	2.058	2.048	2.059	2.052
Ni–N$_B$	2.033	2.032	2.031	2.041
Ni–O$_A$	3.396	3.392	3.409	3.396
Mn–O$_A$–Mn	106.81	106.49	106.45	106.09
O$_B$–Ni–O$_B$	83.80	82.33	81.93	82.23

[a] JT denotes a Jahn−Teller elongation axis. [b] **3*** is a crystallographically independent isomer of **3**.

complexes crystallize as equal mixtures of isomers, with complex **3** being the only one that exhibits two crystallographically unique isomers. All other examples exhibit both isomer types in equal amounts as the result of the glide-plane symmetry operation. Assignments of the Mn^{III} and Ni^{II} oxidation states were made on the basis of charge considerations, the presence of Jahn–Teller (JT) elongation axes, and bond valence sum (BVS) analysis. A summary of the BVS results is given in Table S1 in the Supporting Information. As a generalized example, complex **1** has JT elongation axes determined by the atoms O$_C$ and O$_B$, which correspond to carboxylate and alkoxo O atoms, respectively. The canted

**Table 3.** Selected Bond Distances (Å) and Angles (deg) for Complex **2**[a]

Mn(1)−O(1)	1.884(3)	Mn(3)−O(10) (JT)	2.173(3)
Mn(1)−O(2)	1.941(3)	Mn(3)−N(7)	1.944(4)
Mn(1)−O(3) (JT)	2.402(3)	Ni(1)−O(2)	2.060(3)
Mn(1)−O(6) (JT)	2.170(3)	Ni(1)−O(3)	2.056(3)
Mn(1)−O(7)	1.922(3)	Ni(1)−O(4)	2.084(3)
Mn(1)−N(10)	1.949(4)	Ni(1)−N(1)	2.038(4)
Mn(2)−O(1)	1.898(3)	Ni(1)−N(2)	2.058(4)
Mn(2)−O(3)	1.944(3)	Ni(1)−N(3)	2.046(4)
Mn(2)−O(4) (JT)	2.328(3)	Ni(1)−O(1)	3.376(4)
Mn(2)−O(8) (JT)	2.182(3)	Mn(1)−O(1)−Mn(2)	107.85(14)
Mn(2)−O(9)	1.932(3)	Mn(2)−O(1)−Mn(3)	106.87(14)
Mn(2)−N(4)	1.952(4)	Mn(3)−O(1)−Mn(1)	107.63(14)
Mn(3)−O(1)	1.887(3)	O(2)−Ni(1)−O(3)	84.05(12)
Mn(3)−O(2) (JT)	2.408(3)	O(3)−Ni(1)−O(4)	82.57(12)
Mn(3)−O(4)	1.944(3)	O(4)−Ni(1)−O(2)	82.97(13)
Mn(3)−O(5)	1.935(3)		

[a] JT denotes a Jahn−Teller elongation axis.

orientation of individual JT elongation axes is consistent with the propeller-like hmp$^-$ ligand arrangement and noncentrosymmetric space groups. The shortest metal–oxygen bond distance is that between each Mn^{III} ion and the μ_3-O^{2-} oxide atom, as found in many other oxo-bridged polynuclear Mn complexes.

In addition to the above similarities for these complexes, structural and crystallographic differences among them also exist. The most significant difference among these four complexes is found in the presence or absence of C_3 molecular symmetry. Complexes **1**, **3**, and **4** possess crystallographic C_3 symmetry, whereas complex **2** does not, as detailed below. The lack of C_3 symmetry in **2** has significant effects on its magnetic properties, as will be discussed later.

[Mn$_3$Ni(hmp)$_3$O(N$_3$)$_3$(C$_7$H$_5$O$_2$)$_3$]·2CHCl$_3$ (1). Complex **1**, in which C$_7$H$_5$O$_2$$^-$ is the benzoate anion, crystallizes in the trigonal space group *R*3*c* (No. 161), with the Ni−O$_A$ vectors aligned with the crystallographic *c* axis. The individual JT elongation axes at each Mn^{III} atom are tilted ∼40° from the Mn$_3$ plane, resulting in a net axial anisotropy collinear with the Ni−O$_A$ molecular axis (*c* axis). When the structure is viewed along this axis, there is a symmetry-imposed misalignment of 12.1° between successive Mn$_3$Ni molecules stacked along the C_3 axis. An equal mixture of Δ and Λ isomers is present, as evidenced by the arrangement of the hmp$^-$ chelate rings and ligand substituents and the spiral orientation of the JT elongation axes. Alternating isomeric forms are observed for successive molecules aligned in the *c* direction. The JT axes have Mn−O$_B$ and Mn−O$_C$ bond lengths of 2.375 and 2.177 Å, respectively. The aromatic benzoate rings are twisted 22.7° relative to the Mn–O$_C$–O$_D$ plane, consistent with the handedness of the hmp$^-$ rings, JT axes, and N$_3$$^-$ orientation. In spite of the high crystal diffraction quality, it was not possible to determine the positions of cocrystallized solvent molecules. As a result, SQUEEZE and elemental analysis results were used to determine the existence of two CHCl$_3$ solvate molecules. A stereo view of the crystal packing for complex **1**, neglecting disordered solvate molecules, is given in Figure S3 in the Supporting Information. Thus, there are two CHCl$_3$ solvate molecules packed between neighboring
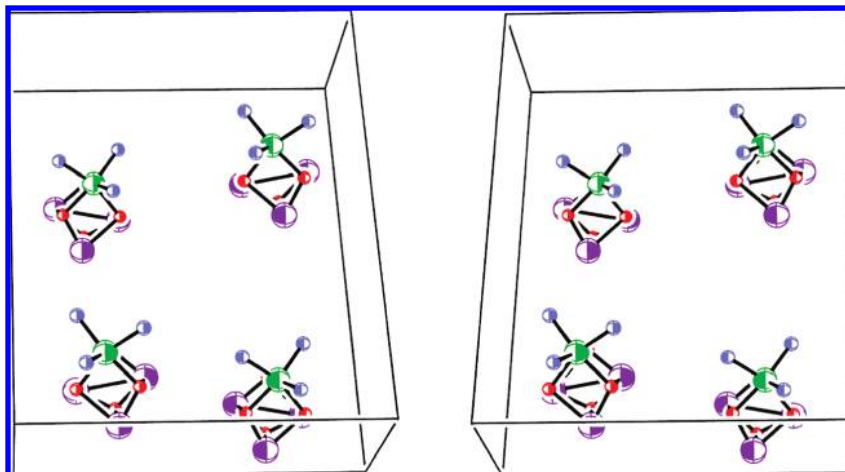
Figure 5. Stereo view of the core cubane structure of complex **2**.

Mn_3Ni complexes, and they are disordered to give an effective C_3 symmetry in the stack.

[Mn₃Ni(hmp)₃O(N₃)₃(C₉H₉O₂)₃] (2). Complex **2**, in which $C_9H_9O_2^-$ is the 3-phenylpropionate anion, crystallizes in the monoclinic space group Cc (No. 9), with no cocrystallized solvate molecules present. Conformational flexibility of the phenylpropionate ligands allows for the observed asymmetric structure. Two of these ligands are oriented with their phenyl rings facing "upward" (toward the Ni^{2+} ion), whereas the third ligand exhibits a downward-facing phenyl ring. This ligand asymmetry imposes C_1 molecular symmetry and results in a lower symmetry space group, as satisfied by the Cc assignment. Geometric asymmetries are further observed within the core structure, notably with respect to the JT elongation axes. The JT axes associated with the upward-facing ligands have the following lengths: $Mn(1)-O(3)$, 2.407 Å; $Mn(1)-O(6)$, 2.167 Å; $Mn(3)-O(2)$, 2.412 Å; and $Mn(3)-O(10)$, 2.173 Å. The JT axis associated with the downward-facing ligand has corresponding bond lengths of 2.332 and 2.182 Å for $Mn(2)-O(4)$ and $Mn(2)-O(8)$, respectively. The asymmetric unit contains a complete molecule, with the c glide plane relating two distinct molecular orientations for Δ and Λ isomers in the crystal structure. The net easy axes between isomers are separated by 14.15° and have a torsion angle of 7.32°, resulting in important implications for single-crystal HFEPR and magnetic studies. This further distinguishes complex **2** from the other analogs, as all of the other complexes except **4** exhibit an alignment of net easy axes in the bulk solid-state structure. These geometric properties are illustrated for the core structure of complex **2** as a stereo view in Figure 5.

[Mn₃Ni(hmp)₃O(N₃)₃(C₁₁H₁₅O₂)₃]·CH₂Cl₂ (3). Complex **3**, in which $C_{11}H_{15}O_2^-$ is the 1-adamantanecarboxylate anion, crystallizes in the hexagonal space group $P6_3$ (No. 173), with one C_3-disordered CH_2Cl_2 molecule per cubane unit. Interestingly, the disordered solvate molecule mimics a $CHCl_3$ molecule, resulting in an occupancy of $^2/_3$ at each C_3-symmetric position. The incorporation of chloroform as a cocrystallized impurity was ruled out on the basis of the electron count from SQUEEZE, replicate crystallizations from pure CH_2Cl_2, and elemental analysis results. Crystal-

lographically independent Δ and Λ isomers were observed in the asymmetric unit. This distinguishes complex **3** from the other analogs, as this represents the only case where the two isomers are not purely related by symmetry. These independent molecules exhibit similar but differing bond geometries. With reference to the atom numbers given in the CIF file in the Supporting Information, the Δ isomer has JT bond lengths of 2.248 and 2.105 Å for $Mn(2)-O(5)$ and $Mn(2)-O(7)$, respectively, while the Λ isomer has JT bond lengths of 2.295 and 2.135 Å for $Mn(1)-O(1)$ and $Mn(1)-O(4)$, respectively. Each isomer is arranged in columns along the crystallographic c axis and has net JT axes collinear with the c axis; adjacent columns contain the other isomeric form. Successive molecules exhibit a 60.5° rotation along this axis. Cubane−solvate interactions are realized through $Cl(2)\cdots N(4)$ (3.083 Å) and $O(2)\cdots C(35)$ (3.156 Å) contacts, resulting in a three-dimensional network encompassing all of the μ_3-O^{2-} ions, azido ligands, and solvate molecules. However, as a result of the C_3 site disorder imposed on the non-C_3 solvate molecule, the exact nature of this interaction cannot be gauged. A stereo view of the unit cell packing for complex **3** is given in Figure 6.

[Mn₃Ni(hmp)₃O(N₃)₃(CH₃CO₂)₃] (4). Complex **4**, in which $CH_3CO_2^-$ is the acetate anion, crystallizes in the cubic space group $I\bar{4}_3d$ (No. 220) with no cocrystallized solvate molecules. The crystals were observed to be dark-red, pyramid-shaped blocks. Four molecular orientations are observed as the result of the intrinsic crystallographic C_2, C_3, and S_4 symmetry operations. These orientations can be observed in Figure S4 in the Supporting Information, where the viewing perspective is near the C_3 rotation axis. Both Δ and Λ isomers are present in **4**, alternating in succession along the C_3 axes. These aligned molecules exhibit an 8.42° rotation between adjacent Mn_3 triangles. However, misalignment of the net JT axes among the four orientations of the molecules leads to bulk compensation for the axial anisotropy, resulting in an isotropic solid-state structure.

Comparison to $S = ^9/_2$ Mn₄ Cubanes. Structural similarities exist between complexes **1−4** and the $S = ^9/_2$ family of Mn_4 SMMs. The most notable similarity is the presence of a triangle of Mn^{III} ions, within which an out-of-plane μ_3-
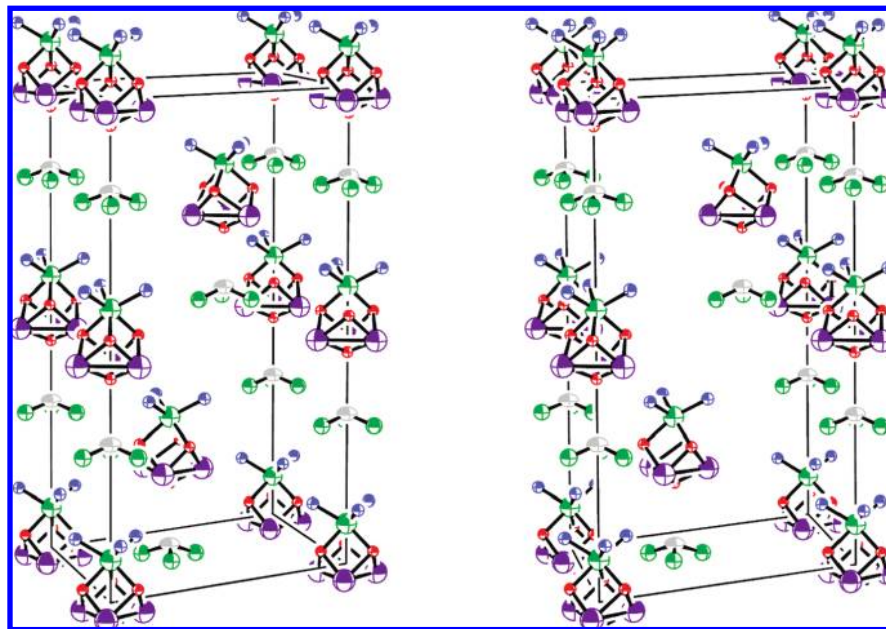
Figure 6. Stereo view of the core cubane structure of complex **3**.

bridging group facilitates ferromagnetic exchange interactions between Mn^{III} ions. The identity of the bridging group is O^{2-} in complexes **1**−**4** and has been varied to include Cl$^-$, Br$^-$, N$_3^-$, NCO$^-$, OH$^-$, or MeO$^-$ in the Mn$_4$ complexes. Substitution of different μ_3-bridging groups results in little change in the magnitude of the ferromagnetic exchange interactions, even as the charge of the bridging group varies from 1− (in the $S = {}^9/_2$ Mn$_4$ complexes) to 2− (in complexes **1**−**4**). Additional discussion of this point is provided below.

The previously studied [Mn$_4$O$_3$X(O$_2$CMe$_3$)$_3$(dbm)$_3$] family [hereafter referred to as Mn$_4$(dbm)] comprises complexes that exhibit C_s and C_{3v} molecular symmetry.[11,38] This contrasts with the C_1 molecular symmetry of complex **2** and C_3 symmetry of complexes **1**, **3**, and **4**. The coordination environment in Mn$_4$(dbm) consists of three dibenzoylmethane anions chelated to three Mn^{III} ions arranged in an equilateral triangle. The dbm$^-$ groups form a conical cavity in which a μ_3-X$^-$ (X$^-$ = Cl$^-$, Br$^-$, N$_3^-$, NCO$^-$, OH$^-$, MeO$^-$) anion resides. This arrangement bears a marked resemblance to what is observed in complexes **1**−**4**, where bound carboxylates form a cavity in which a μ_3-O^{2-} anion bridging the three Mn^{III} ions is located. The apical Mn^{IV} ion in Mn$_4$(dbm) is connected to the Mn$^{III}_3$ triangle through three bridging carboxylate and three μ_3-O^{2-} bridging ions. In comparison, the apical Ni^{II} ion in complexes **1**−**4** is connected to the Mn$^{III}_3$ triangle through three bridging alkoxo groups. The orientations of individual-ion Jahn–Teller elongation axes differ between Mn$_4$(dbm) and complexes **1**−**4**. The JT axes in Mn$_4$(dbm) are described by vectors drawn from the μ_3-X$^-$ anion to each of the three Mn^{III} ions. In contrast, the JT axes in complexes **1**−**4** do not include the μ_3-O^{2-} anion and are more noticeably canted with respect to each other. As a result, complexes **1**−**4** possess smaller individual-ion projections onto the molecular easy axis compared with the

Mn$_4$(dbm) complexes. This is verified quantitatively by the D values for these families, which range from −0.20 to −0.33 cm^{-1} for complexes **1**−**4** in contrast to a range of −0.29 to −0.38 cm^{-1} for Mn$_4$(dbm). Detailed susceptibility and magnetization measurements that were performed in order to further investigate these differences are described below.

Direct-Current Magnetic Susceptibility Studies. Variable-temperature magnetic susceptibility studies were performed on ground crystalline samples of complexes **1**−**4**. The samples were restrained in eicosane to prevent torquing and subjected to a 10 kG field over a temperature range of 1.8–300 K. The data are shown as plots of $\chi_M T$ versus T for complexes **1** and **2** in Figure 7 and for complexes **3** and **4** in Figure S5 in the Supporting Information.

The value of $\chi_M T$ for complex **1** slowly increases from 10.73 cm^3 mol^{-1} K at 300 K to a maximum of 13.60 cm^3 mol^{-1} K at 70 K and then, after a plateau in the 70–20 K range, sharply decreases to 6.24 cm^3 mol^{-1} K at 1.8 K. Complex **2** exhibits similar behavior, with $\chi_M T$ increasing from 10.41 cm^3 mol^{-1} K at 300 K to a maximum value of 12.83 cm^3 mol^{-1}K at 70 K and then decreasing to 6.15 cm^3 mol^{-1} K at 1.8 K. For complex **3**, $\chi_M T$ increases from 9.98 cm^3 mol^{-1} K at 300 K to a maximum of 12.56 cm^3 mol^{-1} K at 70 K and then decreases to a minimum value of 5.77 cm^3 mol^{-1} K at 1.8 K. Complex **4** has a $\chi_M T$ value of 10.90 cm^3 mol^{-1} K at 300 K that increases to a maximum of 13.51 cm^3 mol^{-1} K at 60 K and then decreases to 6.16 cm^3 mol^{-1} K at 1.8 K. The maximum $\chi_M T$ values for complexes **1**−**4** are close to the spin-only ($g = 1.9$) value expected for a complex with an $S = 5$ ground state (13.54 cm^3 mol^{-1} K). Deviations from this $\chi_M T$ value at higher temperatures are due to thermal population of excited states with $S < 5$, while the decreases in $\chi_M T$ at temperatures below ∼20 K likely are due to Zeeman effects, zero-field splitting, or perhaps weak antiferromagnetic exchange interactions between molecules.

(38) Aliaga-Alcalde, N.; Edwards, R. S.; Hill, S. O.; Wernsdorfer, W.; Folting, K.; Christou, G. *J. Am. Chem. Soc.* **2004**, *126*, 12503–12516.
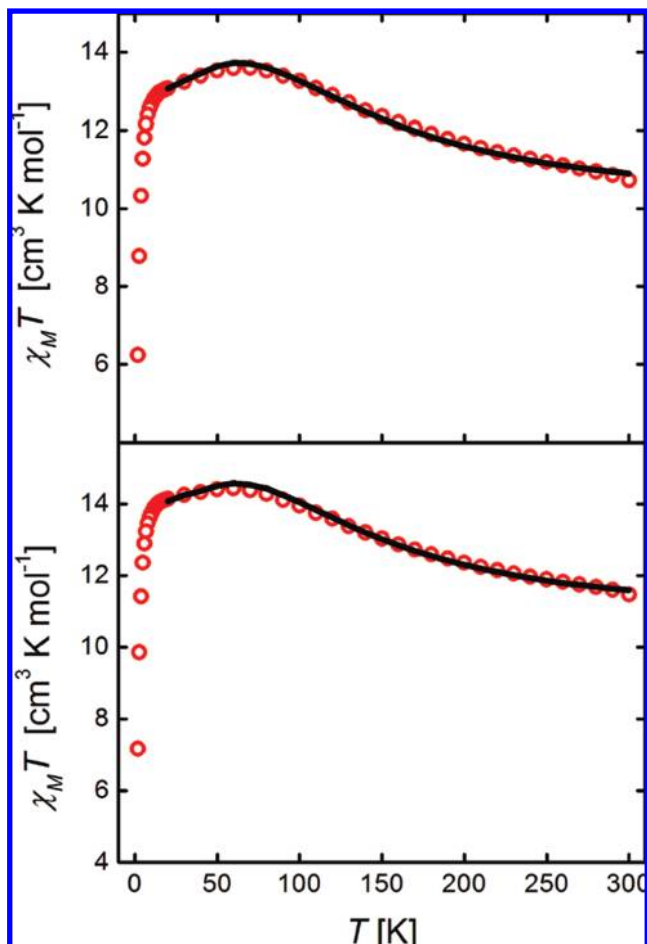
Figure 7. Magnetic susceptibility data taken from 300 to 1.8 K at 10 kG for complexes **1** (top) and **2** (bottom). The best-fit lines (obtained using parameter values given in the text) are shown for 300–20 K.

In order to determine the pairwise exchange interactions within each molecule, the $\chi_M T$ versus T data for complexes **1**−**4** were fit to the spin Hamiltonian $\hat{H}$ given by eq 1:

$$\hat{H} = -2J_{\text{Ni}-\text{Mn}}(\hat{S}_1 \cdot \hat{S}_2 + \hat{S}_1 \cdot \hat{S}_3 + \hat{S}_1 \cdot \hat{S}_4) - \\ 2J_{\text{Mn}-\text{Mn}}(\hat{S}_2 \cdot \hat{S}_3 + \hat{S}_2 \cdot \hat{S}_4 + \hat{S}_3 \cdot \hat{S}_4) \ (1)$$

where the spin of Ni^{II} is $S_1 = 1$, the spins of the three Mn^{III} ions are $S_2 = S_3 = S_4 = 2$, and J_{i-j} is the exchange coupling constant for atoms i and j. In order to solve this Hamiltonian for the appropriate eigenvalue expression, the Kambe vector coupling method was used.[39] In this method, the spin vectors of the three Mn^{III} ions are coupled to give $\mathbf{S}_A = \mathbf{S}_2 + \mathbf{S}_3 + \mathbf{S}_4$, which is then coupled to the Ni^{II} spin vector $\mathbf{S}_1$ to give the total spin vector $\mathbf{S}_T = \mathbf{S}_A + \mathbf{S}_1$. By application of this coupling scheme, eq 1 can be converted to a form that involves only $\hat{S}^2$ operators, from which it is easy to write eq 2, which gives the energy eigenvalues for all of the spin states:

$$E(S_T, S_A) = -J_{\text{Ni}-\text{Mn}}[S_T(S_T + 1) - S_A(S_A + 1)] - \\ J_{\text{Mn}-\text{Mn}}S_A(S_A + 1) \ (2)$$

The overall degeneracy for a $\text{Ni}^{\text{II}}\text{Mn}^{\text{III}}_3$ complex is 375. There are 18 different spin states, over which S_A and S_T vary in

(39) Kambe, K. *J. Phys. Soc. Jpn.* **1950**, *5*, 48.

Table 4. Parameter Values Obtained from Fitting the 10 kG Susceptibility Data and Energies of the First and Second Excited Spin States Relative to the Ground State for Complexes **1**–**4**

parameter	1	2	3	4
g	1.85	1.91	1.88	1.84
$J_{\text{Ni}-\text{Mn}}$ (cm^{-1})	−5.2	−5.2	−5.1	−5.4
$J_{\text{Mn}-\text{Mn}}$ (cm^{-1})	8.3	8.1	8.3	8.7
$E(S_T = 6)$ (cm^{-1})	85.0	60.8	59.7	62.9
$E(S_T = 4)$ (cm^{-1})	112.7	97.4	99.7	103.8

Table 5. Parameter Values and First and Second Excited State Energies Obtained from the Literature for [Mn₄O₃Cl₄(O₂CCH₃)₃(C₅H₅N)₃] [denoted by **Mn₄(Im)**] and [Mn₄O₃Cl(O₂CCH₃)₃(dbm)₃] [denoted by **Mn₄(dbm)**][a]

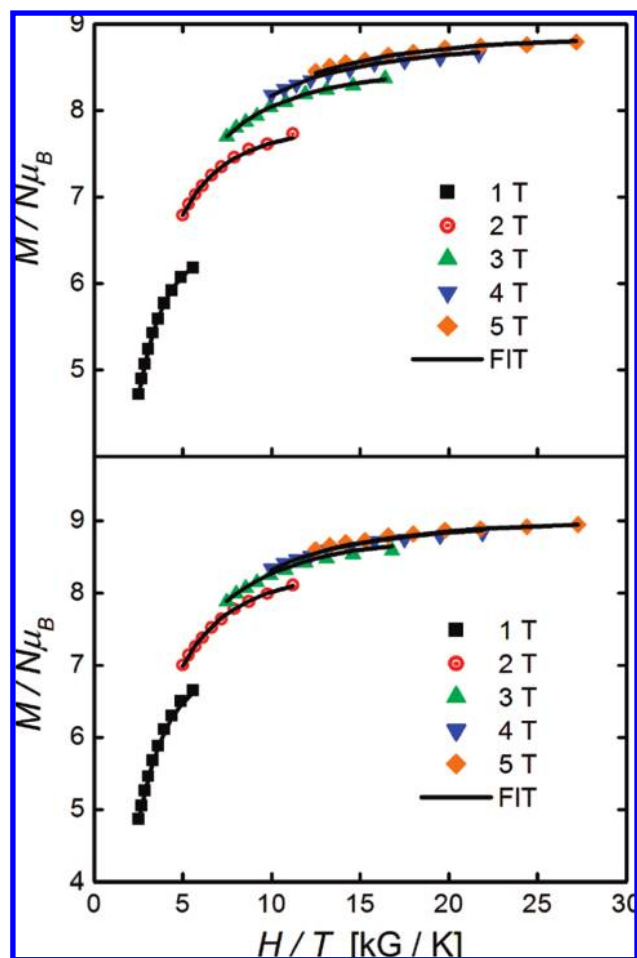| parameter	Mn₄(Im)	Mn₄(dbm)
g	1.86	1.98
$J_{\text{Mn}^{\text{IV}}-\text{Mn}^{\text{III}}}$ (cm^{-1})	−23.1	−28.4
$J_{\text{Mn}^{\text{III}}-\text{Mn}^{\text{II}}}$ (cm^{-1})	11.3	8.3
$E(S_T = 7/2)$ (cm^{-1})	205.4	185
$E(S_T = 11/2)$ (cm^{-1})	254.0	331

[a] Data taken from refs 5 and 11.

integer values from 0 to 6 and 0 to 7, respectively. Substitution of these values into the Van Vleck equation provides a theoretical expression for the molar susceptibility (χ_M) of a $\text{Ni}^{\text{II}}\text{Mn}^{\text{III}}_3$ complex with C_3 symmetry. The exchange Hamiltonian matrix was block-diagonalized using a computer program that incorporates the following parameters: an average g parameter for the Zeeman interactions, $J_{\text{Ni}-\text{Mn}}$, and $J_{\text{Mn}-\text{Mn}}$.[30]

It should be noted that, unlike the other complexes, **2** does not possess rigorous C_3 symmetry. Fitting procedures employing three or four exchange coupling constants yielded parameter values comparable to the two-*J* results but suffered from overparametrization. Further information, such as inelastic neutron scattering data, is required in order to obtain convergence to a unique parameter set.

Although the two-*J* model assumes C_3 symmetry, the Mn₃NiO₄ core of complex **2** is essentially superimposable on the cores of complexes **1**, **3**, and **4**; thus, use of the two-*J* model provides a consistent means of comparing the complexes. The solid lines in Figure 7 and Figure S5 in the Supporting Information represent best fits of the experimental data measured in the 300–20 K range to the theoretical susceptibility equation. The exchange parameter $J_{\text{Ni}-\text{Mn}}$ is characteristic of an antiferromagnetic interaction, ranging from −4.6 to −5.4 cm^{-1} for the series of four complexes, while $J_{\text{Mn}-\text{Mn}}$ has ferromagnetic values ranging from 7.5 to 8.7 cm^{-1}. The values of g, $J_{\text{Ni}-\text{Mn}}$, and $J_{\text{Mn}-\text{Mn}}$ for complexes **1**−**4** are summarized in Table 4. The ground state for each complex is $S_T = 5$ ($S_A = 6$), with first and second excited states of $S_T = 6$ ($S_A = 5$) and $S_T = 4$ ($S_A = 5$), respectively. The energy separations calculated for these excited states relative to the ground state are also given in Table 4 and indicate a reasonably well-isolated ground state. These values are similar to those obtained for two of the $S = 9/2$ Mn₄ cubane complexes, which are summarized in Table 5. The large energy separations between the ground and first excited spin states for the $S = 9/2$ Mn₄ family and complexes **1**−**4** result in well-fit susceptibility and magnetization data, as described below.

Figure 8. Multifield magnetization data for complexes **1** (top) and **2** (bottom) for fields of 1−5 T and temperatures of 1.8–5 K.

Table 6. Best-Fit Parameter Values Obtained from Multifield Magnetization Data for Complexes **1**−**4**[a]

parameter	1	2	3	4
g	1.88	1.89	1.87	1.81
D(cm^{-1})	−0.22	−0.21	−0.33	−0.22
E(cm^{-1})	−	0.005	−	−

[a] A constant TIP value of 4×10^{-4} cm^3 mol^{-1} was used for all fits.

state, fitting of the variable-field magnetization data obtained at 1.8−5 K and 10–50 kG for complexes **1**, **3**, and **4** was performed using the spin Hamiltonian given by eq 3:

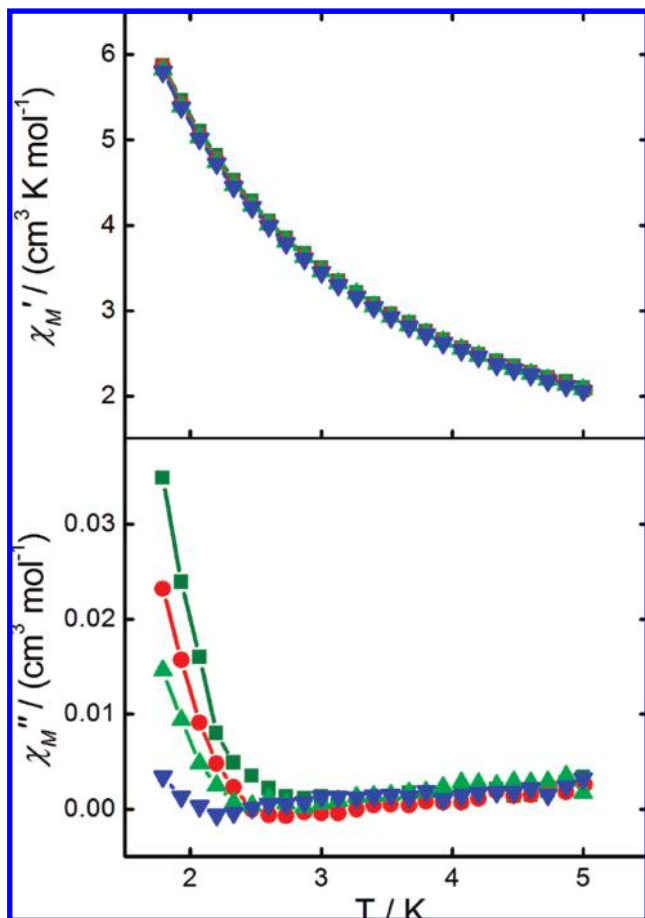$$\hat{H} = D\hat{S}_z^2 + E(\hat{S}_x^2 - \hat{S}_y^2) + g\mu_B\hat{\mathbf{S}}\cdot\mathbf{B} \quad (3)$$

where D is the axial ZFS parameter, E is the rhombic ZFS parameter, $\hat{S}_i$ is the operator for the component of the spin vector, **S**, along the i axis ($i = x, y, z$), g is the Landé g-factor, μ_B is the Bohr magneton, and **B** is the applied magnetic field. This Hamiltonian assumes that only the ground state is populated at these temperatures and magnetic fields and includes isotropic Zeeman interactions and axial ($\hat{D}\hat{S}_z^2$) and rhombic [$E(\hat{S}_x^2 - \hat{S}_y^2)$] ZFS; a full-powder average was calculated.[33] Only the axial ZFS and Zeeman interactions were considered for complexes **1**, **3**, and **4** because of their C_3 crystal site symmetry; that is, the presence of C_3 symmetry precludes rhombic ZFS. The $M/N\mu_B$ versus H/T data for complexes **1**, **3**, and **4** were least-squares fit, and the two 11 × 11 spin Hamiltonian matrices were diagonalized for each setting of the parameters g and D. The resulting eigenvalues, E_i, and their dependencies on the magnetic field, $\delta E_i/\delta B$, were used to calculate the magnetization according to eq 4:

$$M = N\sum_i \left(\frac{\delta E_i}{\delta B}\right) \exp(-E_i/kT) / \sum_i \exp(-E_i/kT) \quad (4)$$

where k is the Boltzmann constant. Good fits to an $S = 5$ ground state were achieved, as illustrated by the solid lines in Figures 8 and S6, while fits to $S = 4$ and $S = 6$ ground states yielded very large fitting errors and unreasonable values of g (1.6 or −0.54) and D (0.027 or −0.022 cm^{-1}). A fixed temperature-independent paramagnetism (TIP) value of 4×10^{-4} cm^3 mol^{-1} was used for all of the complexes. Table 6 summarizes the best-fit parameter values for complexes **1**−**4**. Two fitting minima were obtained for each complex, corresponding to fits with negative and positive D values, but the fits with negative D values were found to be better. HFEPR spectra confirmed that $D < 0$. Because complex **2** has C_1 site symmetry, the rhombic ZFS term $E(\hat{S}_x^2 - \hat{S}_y^2)$ was included in the fitting of its reduced magnetization data using the spin Hamiltonian given in eq 3. Fitting of the experimental data resulted in a good fit with parameter values of $g = 1.89$, $D = -0.21$ cm^{-1}, and $E = 0.005$ cm^{-1}.
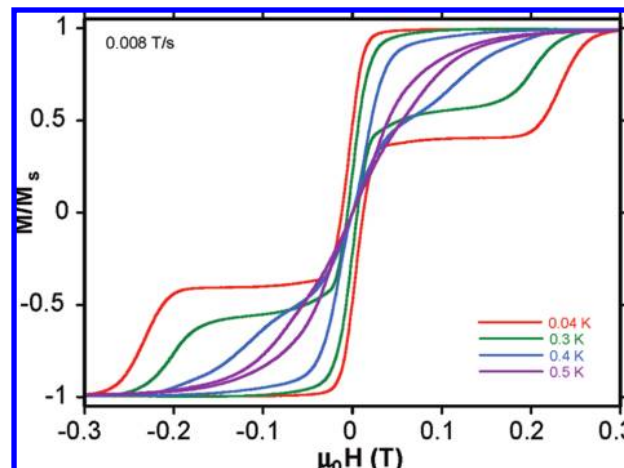
Alternating-Current Magnetic Susceptibility Studies. Alternating-current susceptibility measurements were performed over a temperature range of 1.8–5 K using a 3.0 G ac field oscillating at frequencies of 50–997 Hz. If the net magnetization relaxes fast enough to keep up with the oscillating ac field, then there is no imaginary (out-of-phase) susceptibility (χ''_M) and the real (in-phase) susceptibility (χ'_M) is equal to the dc susceptibility. However, if the effective barrier to magnetization relaxation is significant in compari-

Studies of Magnetization as a Function of Magnetic Field. The above analysis of the susceptibility data, which employs the eigenvalues from eq 2 and the Van Vleck equation, does not account for Zeeman interactions at low temperatures or the effects of zero-field splitting. As a result, magnetization data as a function of dc field were collected for samples of **1**−**4** in order to evaluate the magnitude of the ZFS parameter D and confirm the $S_T = 5$ spin ground state. Ground crystalline samples were embedded in eicosane to prevent torquing of the magnetically anisotropic particles and subjected to fields of 10–50 kG over a temperature range of 5–1.8 K. Plots of reduced magnetization $M/N\mu_B$, where M is the molar magnetization, N is Avogadro's number, and μ_B is the Bohr magneton, versus H/T are shown for complexes **1** and **2** in Figure 8 and complexes **3** and **4** in Figure S6 in the Supporting Information. At the lowest measured temperature (1.8 K) and highest field (50 kG), $M/N\mu_B$ saturates at values close to 9, which is less than the $M/N\mu_B$ value of $gS = 10$ expected for an $S = 5$ complex experiencing no zero-field splitting. Furthermore, it is clear that the five isofield curves for each complex do not superimpose, indicating that each of these complexes experiences zero-field interactions.

Since fitting of the 10 kG variable-temperature magnetic susceptibility data indicates a well-isolated $S = 5$ ground

Figure 9. (top) In-phase and (bottom) out-of-phase ac susceptibility data for complex **1**.

Figure 10. Temperature-dependent hysteresis loop measurements for a single crystal of **1**. The magnetization is normalized by the saturation value M_s.

son to the thermal energy (kT), then a nonzero χ''_M value is seen, accompanied by a concomitant decrease in χ'_M. If such a magnetization reversal barrier exists, then χ'_M and χ''_M are also frequency-dependent. Frequency dependence of the out-of-phase ac susceptibility is a characteristic property of SMMs, though it is also expressed in materials such as spin-glasses below their transition temperature.[40,41] For complexes **1**, **2**, and **3**, the in-phase susceptibility value extrapolated to 0 K is 12–13 cm³ mol⁻¹ K, which is slightly less than the value of 14–15 cm³ mol⁻¹ K expected for an $S = 5$ ground state with $g < 2$. This smaller value may be attributed to the presence of weak intermolecular antiferromagnetic exchange interactions and/or the effects of anisotropy at low temperatures. The χ'_M and χ''_M plots for **1**, **2**, and **3**, respectively, are shown in Figure 9 and Figures S7 and S8 in the Supporting Information. The out-of-phase susceptibilities for **1**, **2**, and **3** have very small magnitudes with respect to the in-phase signals. The strongest χ''_M signal is that of **3**, which corresponds to 3.1% of χ'_M at 997 Hz and 1.8 K. Under the same conditions, complexes **1** and **2** have out-of-phase signals that, at the lowest temperatures, are 0.6% of their respective in-phase components. These observations make qualitative sense in view of the magnitudes of D for

these complexes: **1** and **2** have comparable D values that are significantly smaller than that for **3**. The χ''_M signal for complex **2** approaches an apparent peak maximum at 1.8 K for ac fields of 997 and 750 Hz; the peak maxima for all of the other complexes clearly are located at temperatures well below 1.8 K.

In light of the small relative χ''_M values at low temperatures, the presence of these frequency-dependent ac susceptibility signals suggests that complexes **1**–**4** may behave as SMMs. To investigate this possibility, single-crystal hysteresis measurements at temperatures reaching 0.04 K were performed using a micro-SQUID instrument.[20,42]

Hysteresis Loops in Plots of Single-Crystal Magnetization versus Field. Given the predispositions of these complexes for SMM behavior, such as the $S = 5$ ground states, negative D values, and out-of-phase ac susceptibility signals, scans of magnetization versus applied dc field were conducted for single crystals of complexes **1**, **2**, and **3** using a micro-SQUID magnetometer.[20,42] Complex **4** was not studied because of the nearly isotropic molecular arrangement in its solid-state structure. Experiments were conducted under two sets of conditions: (1) a 0.008 T s⁻¹ field sweep rate and a temperature range of 0.04–1.1 K (Figures 10–12) and (2) a temperature of 0.04 K and field sweep rates of 0.008–0.140 T s⁻¹ (Figures S9–S11 in the Supporting Information). Hysteresis loops were observed for these complexes, indicating that they function as SMMs.

A single easy-axis orientation for complexes **1** and **3** allowed for application of the external magnetic field along the molecular c axis. The resulting hysteresis curves are characterized by temperature and sweep-rate dependence, a small coercive field, and the presence of vertical steps in the curves. The first step observed in sweeping the field from one saturating value to another occurs at zero field, where the potential energy double well is degenerate (in resonance). The steps are positions of increased magnetization relaxation rate, corresponding to tunneling through an anisotropy
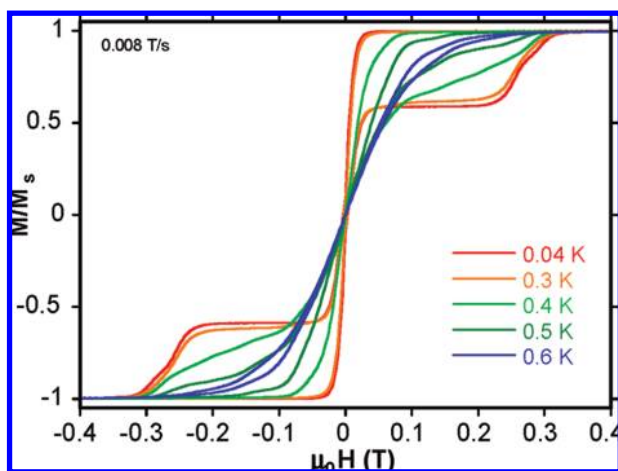
(40) Prokofev, N. V.; Stamp, P. C. E. *J. Low Temp. Phys.* **1998**, *113*, 1147–1152.

(41) Gao, S.; Su, G.; Yi, T.; Ma, B. Q. *Phys. Rev. B* **2001**, *63*, 054431.

(42) Bouchiat, V.; Faucher, M.; Thirion, C.; Wernsdorfer, W.; Fournier, T.; Pannetier, B. *Appl. Phys. Lett.* **2001**, *79*, 123–125.
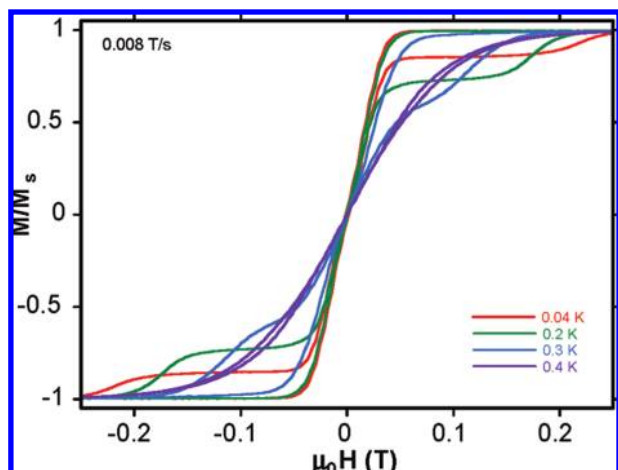
Figure 11. Temperature-dependent hysteresis loop measurements for a single crystal of **2**. The magnetization is normalized by the saturation value M_s.

Figure 12. Temperature-dependent hysteresis loop measurements for a single crystal of **3**. The magnetization is normalized by the saturation value M_s.

barrier. These vertical steps are a diagnostic signature of QTM, and their periodic separation ΔH is proportional to the ZFS parameter D according to eq 5:

$$\Delta H = \frac{k|D|}{g\mu_0\mu_B \cos(\alpha)} \tag{5}$$

where α is the bisecting angle between the applied dc field and the easy axis of the molecule; in the case of **1** and **3**, $\alpha = 0$.[19,43,44] The large step near $H = 0$ indicates fast quantum tunneling at zero field, as expected for a non-Kramers-degenerate $S = 5$ complex.[45–48] The vertical step at approximately ± 0.2 T corresponds to QTM from the $m_S = +5$ ground state through the anisotropy barrier to the $m_S =$

(43) Friedman, J. R.; Sarachik, M. P.; Tejada, J.; Maciejewski, J.; Ziolo, R. *J. Appl. Phys.* **1996**, *79*, 6031–6033.
(44) Sangregorio, C.; Ohm, T.; Paulsen, C.; Sessoli, R.; Gatteschi, D. *Phys. Rev. Lett.* **1997**, *78*, 4645–4648.
(45) Leuenberger, M. N.; Loss, D. *Phys. Rev. B* **2001**, *63*, 054414.
(46) Wang, S. Y.; Wemple, M. S.; Yoo, J.; Folting, K.; Huffman, J. C.; Hagen, K. S.; Hendrickson, D. N.; Christou, G. *Inorg. Chem.* **2000**, *39*, 1501–1513.
(47) Wang, S. Y.; Tsai, H. L.; Hagen, K. S.; Hendrickson, D. N.; Christou, G. *J. Am. Chem. Soc.* **1994**, *116*, 8376–8377.
(48) Aromí, G.; Bhaduri, S.; Artus, P.; Folting, K.; Christou, G. *Inorg. Chem.* **2002**, *41*, 805–817.

-4 state (where m_S is the quantum number for the projection of **S** onto the magnetic quantization axis). The large QTM rate explains the narrow coercive field at $M/M_s = 0$ for complexes **1**–**3**. In contrast, the $S = {}^9/_2$ family of C_{3v}-symmetric Mn$_4$ cubanes exhibit a large coercive field at $M/M_s = 0$ as a result of their half-integer spin ground states. It is important to note that the axial C_3 symmetry of complexes **1** and **3** seemingly precludes the presence of the rhombic ZFS interaction $E(\hat{S}_x^2 - \hat{S}_y^2)$. The rhombic term, which equals zero in axial symmetry, represents a source of state mixing on either side of the energy barrier, leading to the occurrence of QTM. Complexes that exhibit low symmetry possess larger rhombic terms, resulting in increased state mixing and larger QTM rates. This has been directly observed in Mn$_4$ examples (Figures S12 and S13 in the Supporting Information) and in complexes **1**–**3** (Figures 10−12), where reducing the symmetry from C_3 to C_1 leads to larger tunneling rates. Because mixing due to off-diagonal terms in the spin Hamiltonian accounts for QTM, the lack of an E term in complexes **1** and **3** suggests a different source of mixing leading to QTM. The existence of disordered solvate molecules in the lattices of complexes **1** and **3** likely contributes to the observation of fast QTM in these molecules. However, it is also possible that the fast tunneling arises from higher-order ZFS interactions.

Because complex **2** assumes two molecular orientations in the solid-state crystalline structure, the external field was applied halfway between the net easy axes, at an angle of $\alpha \approx 7°$. Application of eq 5 to the hysteresis data of complex **2** yielded a calculated D value of -0.21 cm^{-1}, in good agreement with the value of -0.21 cm^{-1} derived from fitting the variable-field magnetization data. As mentioned previously, complex **2** differs from complexes **1** and **3** in that it does not exhibit C_3 symmetry. This has implications for the magnetization relaxation properties, namely, the presence of the rhombic ZFS term $E(\hat{S}_x^2 - \hat{S}_y^2)$ in eq 4 and the origin of QTM. As expected, complex **2** exhibits a smaller coercivity and larger rate of QTM than complexes **1** and **3**. In fact, the rate of quantum tunneling for complex **2** is so large that there appears to be very little coercivity at $M/M_s = 0$. The SMM character of **2** is established by the observed temperature and sweep-rate dependence of the hysteresis loops. These results are consistent with hysteresis data for $S = {}^9/_2$ Mn$_4$, for which lower-symmetry complexes yielded larger tunneling rates than their higher-symmetry analogues. Magnetization hysteresis loops for these Mn$_4$ examples are shown in Figures S12 and S13 in the Supporting Information. Considering the significant impact that the symmetry and the rhombic anisotropy have on QTM rates, HFEPR spectroscopy was employed to reliably characterize the magnitudes and signs of the spin Hamiltonian parameters.

Single-Crystal HFEPR Spectroscopy. Single-crystal HFEPR spectroscopy has become an important tool for studying systems with high-spin ground states that exhibit significant magnetoanisotropy. While magnetization measurements based on polycrystalline bulk magnetic susceptibility data yield reasonable estimates of Hamiltonian parameter values, HFEPR can unambiguously determine the

spin of the ground state[49] as well as the sign and magnitude
of the axial ZFS parameter D.[50] Most notably, it is a vital
tool for characterizing transverse ZFS terms {e.g., the
rhombic $[E(\hat{S}_x^2 - \hat{S}_y^2)]$ and fourth-order $(B_4^4\hat{O}_4^4)$ terms}.[51] The
presence of transverse terms gives rise to the mixing of m_S
states of opposite projection that leads to QTM.[52,53] Minima
observed in the HFEPR spectra result from magnetic-dipole
transitions between ground-state spin sublevels whose m_S
values differ by ±1 (i.e., $-5 \rightarrow -4$, $-4 \rightarrow -3$, etc.). Since
there are $2S + 1$ sublevels, the number of such transitions is
$2S$; for the isotropic case (no ZFS), these transitions are
degenerate, and only a single EPR peak is observed.
However, to a first approximation, anisotropic terms in the
Hamiltonian (e.g., ZFS) split the spectrum into $2S$ discrete
peaks. If both the spin, S, and the magnetoanisotropy are
large, then strong magnetic fields (B) and high frequencies
(f) may be needed to resolve all $2S$ of these transitions.[54]
By recording the spectra as a function of temperature, one
can determine the absolute sign of D on the basis of the
thermal populations of m_S levels inferred from the
spectra.[55,56]

A general Hamiltonian, similar to eq 3 but expanded to
include higher-order ZFS terms, is given by eq 6:

$$\hat{H} = \mu_B\hat{\mathbf{S}}\cdot\mathbf{g}\cdot\mathbf{B} + D\hat{S}_z^2 + E(\hat{S}_x^2 - \hat{S}_y^2) + B_4^0\hat{O}_4^0 + \hat{O}_{4,6}^T + \hat{H}' \quad (6)$$

The first three terms in this equation are the same as those
previously described in eq 3; the next term represents fourth-
order axial anisotropy (the operator $\hat{O}_4^0$ contains $\hat{S}_z^4$), which
we have found to be significant for these complexes; the
fifth term represents possible higher-order (fourth- and sixth-
order) contributions to the transverse anisotropy; and finally,
the last term, $\hat{H}'$, parametrizes all other perturbations (e.g.,
dipolar and intermolecular exchange interactions).

In order to locate the easy (z) axis and hard (xy) plane of
complex **1**, a face-indexed single crystal was carefully
oriented within a cylindrical TE_{01n} mode cavity so that angle-
dependent HFEPR measurements could be performed with
field rotation in a plane inclined reasonably close to the
estimated easy-axis direction. Angle-dependent data obtained
at 110 GHz (Figure S14 in the Supporting Information)
exhibit twofold behavior consistent with the axial crystal-
lographic symmetry. To exactly locate the hard plane, fine
angle-dependence measurements (2° steps) centered around
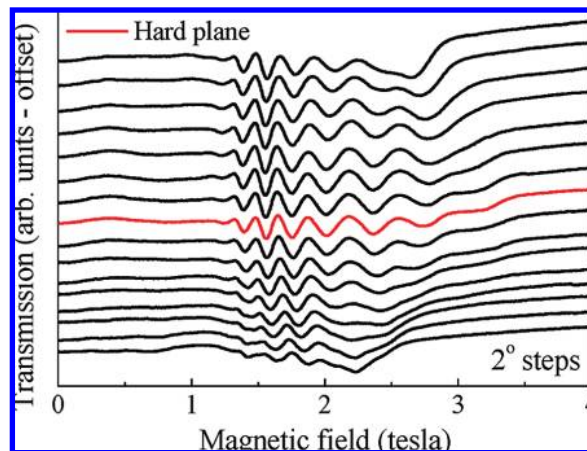
Figure 13. Angle-dependent HFEPR spectra (2° steps) for complex **1** at
50.9 GHz and 5 K. The angle at which the red spectrum was recorded
corresponds to the hard plane.
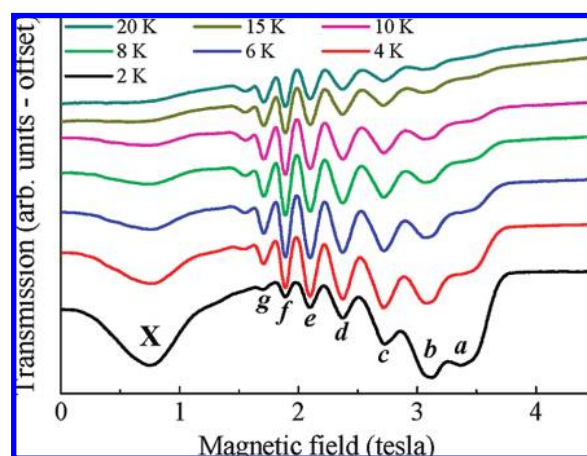
Figure 14. Temperature-dependent HFEPR spectra for the hard plane of
complex **1** from 2 to 20 K at 59.9 GHz. The transition peaks are labeled as
a, **b**, **c**, **d**, **e**, **f**, **g**, and **X** (see the text and Figure 15 for details).

the estimated hard plane direction were performed at 50.9
GHz and 5 K, as shown in Figure 13.

Figure 14 illustrates the hard-plane temperature depen-
dence of the spectrum of **1** collected over a temperature range
of 2−20 K at 59.9 GHz. As the temperature decreases, the
thermal (Boltzmann) weighting of the spectrum shifts toward
transitions occurring at higher magnetic fields, as expected
for a system with a negative D value. The peak assignments
(refer to the Figure 14 caption) are based on the energy level
diagram in Figure 15, which was generated using the ZFS
parameters obtained as described above; the labeling corre-
sponds to a high-field limit ($g\mu_B B > |DS|$) in which m_S
represents the projection of the spin onto the applied
magnetic field axis (see the right side of Figure 15). Even at
the lowest temperature (2 K), significant populations exist
among excited m_S levels as a result of the relatively weak
ZFS in this complex.

The spectra in Figure 14 exhibit considerable asymmetry
and line broadening that increase for transitions occurring
at higher magnetic fields. HFEPR studies of many other
polynuclear transition metal complexes have shown that such
m_S dependence of the line shapes and widths is caused by
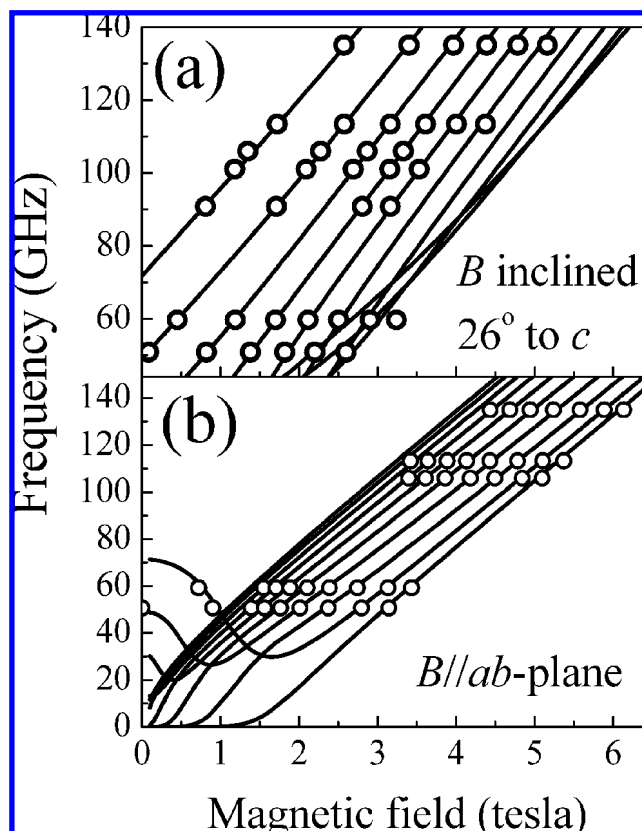disorder, often involving the ligand groups and/or solvate

(49) Edwards, R. S.; Hill, S.; Bhaduri, S.; Aliaga-Alcalde, N.; Bolin, E.; Maccagnano, S.; Christou, G.; Hendrickson, D. N. *Polyhedron* **2003**, *22*, 1911–1916.
(50) Rumberger, E. M.; Hill, S.; Edwards, R. S.; Wernsdorfer, W.; Zakharov, L. N.; Rheingold, A. L.; Christou, G.; Hendrickson, D. N. *Polyhedron* **2003**, *22*, 1865–1870.
(51) Gatteschi, D.; Sessoli, R. *Angew. Chem., Int. Ed.* **2003**, *42*, 268–297.
(52) Hill, S.; Edwards, R. S.; Jones, S. I.; Dalal, N. S.; North, J. M. *Phys. Rev. Lett.* **2003**, *90*, 217204.
(53) Hill, S.; Maccagnano, S.; Park, K.; Achey, R. M.; North, J. M.; Dalal, N. S. *Phys. Rev. B* **2002**, *65*, 224410.
(54) Hill, S.; Perenboom, J. A. A. J.; Dalal, N. S.; Hathaway, T.; Stalcup, T.; Brooks, J. S. *Phys. Rev. Lett.* **1998**, *80*, 2453–2456.
(55) Collison, D.; Murrie, M.; Oganesyan, V. S.; Piligkos, S.; Poolton, N. R. J.; Rajaraman, G.; Smith, G. M.; Thomson, A. J.; Timko, G. A.; Wernsdorfer, W.; Winpenny, R. E. P.; McInnes, E. J. L. *Inorg. Chem.* **2003**, *42*, 5293–5303.
(56) McInnes, E. J. L.; Piligkos, S.; Timco, G. A.; Winpenny, R. E. P. *Coord. Chem. Rev.* **2005**, *249*, 2577–2590.
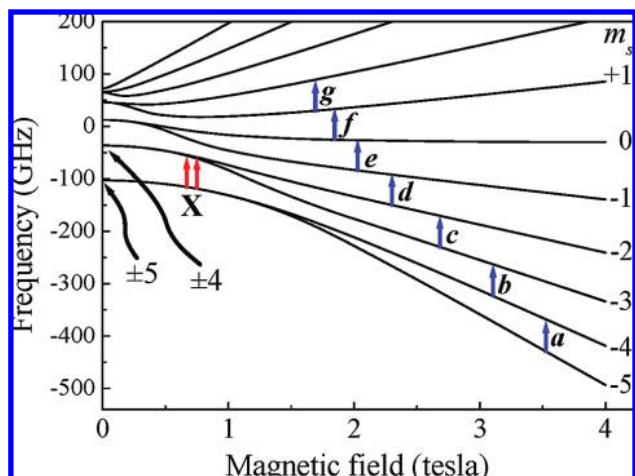
Figure 15. Energy level diagram for the hard plane of complex **1**. The blue upward-pointing arrows indicate the EPR transitions labeled **a**–**g** in Figure 14, and the red upward-pointing arrows indicate the EPR transition labeled **X**.

molecules.[17,49] This leads to inhomogeneous distributions of the local **g** and **D** tensors, giving rise to so-called g- and D-strain.[4,57–60] In particular, it has been well documented that D-strain, as well as small distributions (with widths of <1°) in the orientations of the local magnetic easy axes, can cause asymmetries in the hard-plane spectra such as those seen in Figure 14. D-strain induces broadening that depends linearly on the absolute value of m_S associated with the level from which a given transition is excited, i.e., the line width increases with increasing $|m_S|$. Since the overall peak area must be conserved, peak intensity (height) is lost as a result of this line broadening. In light of this, we can account for the overall trends observed in the temperature-dependent data in Figure 14. First of all, the peaks near the center of the spectrum (**e**, **f**, and **g**), which are associated with the smallest $|m_S|$ values, are considerably sharper than the highest-field peaks. This result, combined with the fact that the associated transition probabilities [which are proportional to $(S + m_S + 1)(S - m_S)$] are also stronger for transitions originating from smaller-$|m_S|$ states, leads to a situation in which the central peaks dominate the spectrum in the high-temperature limit in which the Boltzmann weights are quite similar for all of the transitions. In the low-temperature limit, the spectral weight shifts to high fields. Nevertheless, the transition originating from the ground state (**a**: $m_S = -5$ to -4) remains weaker than that from the first excited state (**b**: $m_S = -4$ to -3) at 2 K for the reasons discussed above.

An interesting feature in Figure 14 is the broad temperature-dependent peak (labeled **X**) at ~0.7 T. The origin of the peak can clearly be seen in Figure 15 (indicated by red arrows). In the zero-field limit, the two lowest-lying doubly degenerate levels correspond to $m_S = \pm 5$ and ± 4, where m_S

(57) Park, K.; Novotny, M. A.; Dalal, N. S.; Hill, S.; Rikvold, P. A. *Phys. Rev. B* **2002**, *65*, 014426.
(58) Maccagnano, S.; Achey, R.; Negusse, E.; Lussier, A.; Mola, M. M.; Hill, S.; Dalal, N. S. *Polyhedron* **2001**, *20*, 1441–1445.
(59) Park, K.; Novotny, M. A.; Dalal, N. S.; Hill, S.; Rikvold, P. A. *J. Appl. Phys.* **2002**, *91*, 7167–7169.
(60) Parks, B.; Loomis, J.; Rumberger, E.; Hendrickson, D. N.; Christou, G. *Phys. Rev. B* **2001**, *64*, 184426.
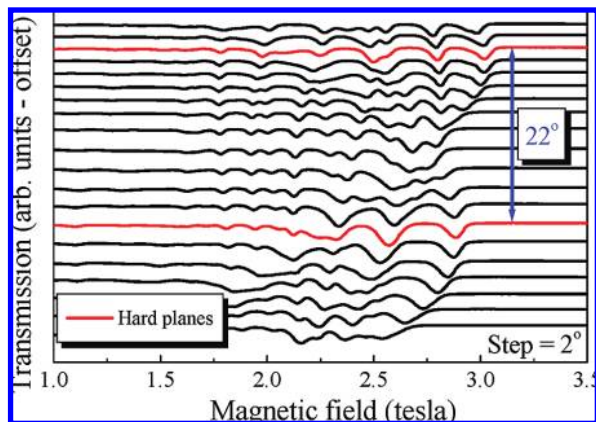
Figure 16. Frequency-dependent HFEPR peak positions for complex **1** between 50 and 135 GHz with the field (a) close to the easy axis and (b) precisely aligned with the hard plane. The solid curves represent the best simulations of the experimental data (see the text for parameter values used).

now refers to the spin projection onto the molecular easy (z) axis. As inspection of Figure 15 shows, these levels converge but then ultimately repel upon application of a transverse magnetic field; their separation reaches a minimum at 1.7 T. The 0.7 T peak corresponds to the transitions between these levels, as indicated by the red arrows at ~0.7 T in Figure 15. There are several factors that contribute to the broad nature of this peak. First, as a result of the considerable mixing of m_S states for $B \perp z$ (and for $g\mu_B B \approx |DS|$), the absorption at 0.7 T actually corresponds to multiple transitions between the four lowest-lying levels, which are not quite degenerate in this field range. Second, the nonlinear field dependence of the EPR frequencies (due to separations between the $m_S = \pm 5$ and ± 4 states) associated with these transitions tends to broaden the resonance peak on the low-field side. Third, because the spin projections associated with the states involved in these transitions are large (i.e., $m_S \approx \pm 5$ and ± 4), the D-strain is also large for this peak.

Frequency-dependence studies were carried out on complex **1** between 50 and 135 GHz with the field (a) close to the easy axis and (b) precisely aligned in the hard plane; the positions of the EPR peaks observed for these two orientations at various frequencies are plotted in panels a and b, respectively, of Figure 16. The solid curves represent the best simulations of the data obtained via exact diagonalization of eq 6 using the following parameter values: $S = 5$, $D = -0.23$ cm^{-1}, $B_4^0 = -5.68 \times 10^{-5}$ cm^{-1}, $g_z = 2.02$, and $g_x =$

Figure 17. Angle-dependent HFEPR spectra (2° steps) for complex **2** at 55.2 GHz and 3 K. The angles of the red spectra correspond to the hard-plane orientations, which are separated by ~22°.


Figure 18. Plot of the positions of the highest-field peaks in Figure 17 as a function of angle for complex **2**. The values of the peak positions at the maxima differ by 0.15 T. The two hard-plane directions are given by the angles at which the maxima occur.

$g_y = 1.95$. This single set of parameter values gives good overall agreement with the data obtained for both orientations and does not require the inclusion of transverse ZFS parameters for the hard plane. While this does not conclusively rule out the presence of transverse ZFS terms (indeed, they must be present in order to explain the QTM), it suggests that they must be rather weak, a finding which is consistent with the high symmetry (C_3) of complex **1**. Similar results were obtained for mixed-valence high-symmetry (C_{3v}) $Mn^{IV}Mn^{III}_3$ cubane complexes.[38] It is also worth noting that the values for the fourth-order axial ZFS parameter, B_4^0, obtained for complexes **1** and **2** (described above) are essentially identical to those obtained for the $Mn^{IV}Mn^{III}_3$ cubane complexes, even though the D values for the present heterometallic systems are significantly smaller (D is on the order of -0.5 cm^{-1} for a typical high-symmetry Mn₄ complex). At present, we do not understand the significance of this finding. Finally, we note that the simulation in Figure 16a required the inclusion of a significant tilt angle of 26° between **B** and z, indicating that our attempts to align the sample within the cavity were not entirely successful. Nevertheless, the ability to obtain multifrequency HFEPR data for two distinct field orientations (i.e., parallel and approximately perpendicular to the hard plane) provides considerable constraints on the values obtained for the ZFS parameters.

Angle-dependence data for complex **2** were recorded at two sets of frequency and temperature conditions: (102.8 GHz, 2 K) and (55.2 GHz, 3 K). The spectra for this complex are complicated by the fact that two molecular orientations (Δ and Λ isomers) exist within the unit cell. Thus, after an initial coarse angle-dependence measurement (15° steps) was performed under the first set of conditions (Figure S15 in the Supporting Information), measurements were performed under the second set of conditions using finer angle steps (2°) close to the suspected hard-plane orientations. A series of such spectra are displayed in Figure 17, and the position of the highest-field peak is plotted versus angle (with arbitrary offset) in Figure 18. Two hard directions are clearly visible from the two peak-position maxima, which are separated by 22° (Figure 18).
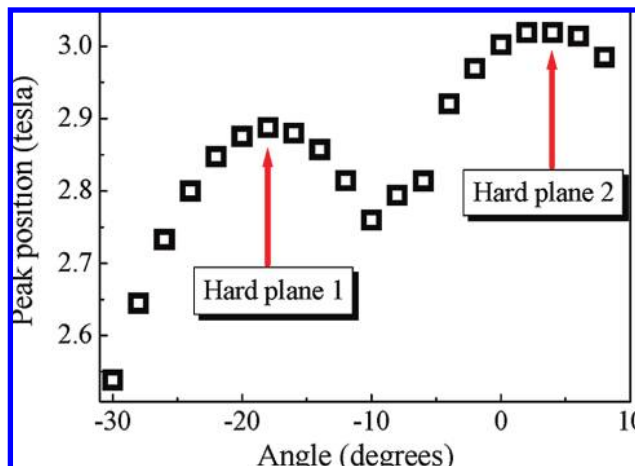
The presence of two distinct hard planes is consistent with the crystallographic structure of complex **2**. Molecules having Cc space group symmetry are related by the symmetry operations x, $-y$, $½ + z$, and the glide plane in c leads to a 14.15° angle between the easy-axis orientations of the two symmetry-related molecules as well as a torsion angle of 7.32°. A particularly notable feature of the angle-dependence studies close to the two hard planes is the fact that there is a roughly 0.15 T field separation between the two maxima in Figure 18. One explanation for this result might be that the ZFS parameters for the isomers differ slightly. However, as noted above, the two sites are related by a simple symmetry operation, thus ruling out this possibility. The most plausible explanation involves transverse anisotropy, which could be appreciable for this low-symmetry space group. While we again attempted to align the sample in the cavity prior to cooling, we can infer that the plane of field rotation was significantly tilted relative to the easy axes associated with the two isomers, i.e., it was not orthogonal to either hard plane. This fact can account for two key features of the resulting data: (a) the 0.15 T field separation of the maxima in Figure 18 and (b) the fact that the experimental separation between angles of these maxima is 22°, whereas the X-ray data suggest that the orientations of the two isomers differ by only 14.15°. The latter observation finds a natural explanation in terms of an inclined field rotation plane; indeed, one would expect to observe a precise angle separation of 14.15° only for the situation in which the field intersects both hard planes in a mutually orthogonal plane of rotation.

The local C_3 axial symmetry imposed on complex **1** is lifted for the C_1 molecular site symmetry of complex **2**, resulting in the presence of a rhombic $E(\hat{S}_x^2 - \hat{S}_y^2)$ term (as well as many higher-order terms) in the Hamiltonian for **2**. In addition, the easy-axis tilt angle between the two isomers likely enhances the transverse anisotropy, leading to larger rates of QTM for complex **2**, as observed from the aforementioned magnetization hysteresis loops. Because of the inclination of the field rotation plane inferred from the
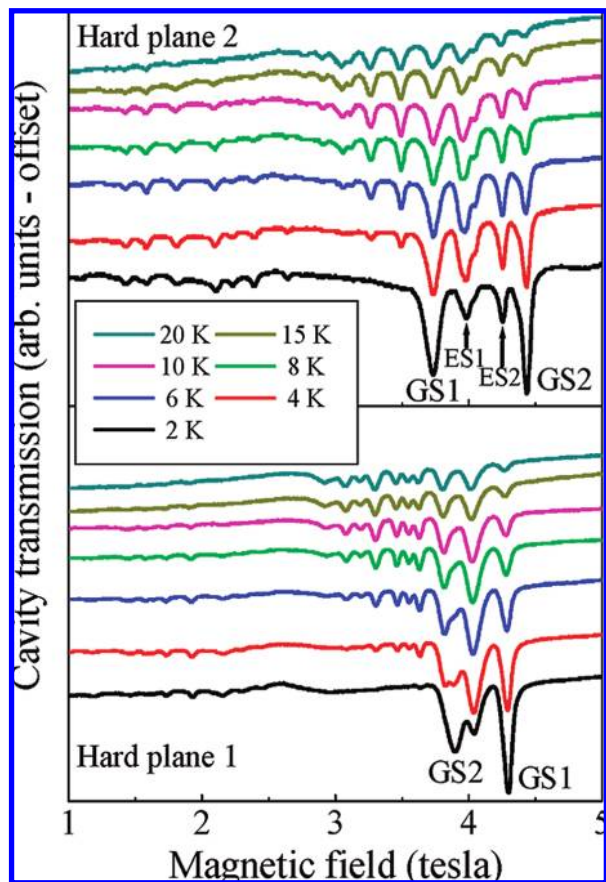
Figure 19. Temperature-dependent hard-plane spectra for complex **2** at 94.8 GHz and 2−20 K, with the field aligned parallel to the hard plane of isomers 1 (bottom) and 2 (top). Peaks corresponding to the ground-state (GS) and first excited-state (ES) transitions of the two isomers are assigned. Double-quantum transitions ($\Delta m_S = \pm 2$) are clearly evident below 3 T.

angle-dependence measurements, it is likely that the field intersects the two hard planes at different locations within the respective local xy coordinate frames associated with the two isomers. This fact, combined with a transverse anisotropy term, would then result in different spacings between the hard-plane peaks observed for the two isomers, leading to the 0.15 T difference between the maxima in Figure 18. Therefore, the angle-dependence studies provide clear evidence for a significant transverse anisotropy associated with complex **2**, which we attempt to deduce below.

Figure 19 displays temperature-dependent hard-plane spectra obtained at 94.8 GHz for the two estimated hard-plane orientations. As in the spectra of complex **1**, the spectral weight shifts toward the high-field peaks as the temperature decreases, again signifying a negative axial anisotropy (i.e., $D < 0$). However, in the present case, two strong peaks appear in the limit of low temperature, corresponding to the two isomers with their different orientations. These two peaks, which correspond to the transitions from the ground states of the isomers (nominally $m_S = -5$), have been labeled GS1 and GS2 in Figure 19; GS1 (GS2) is seen at higher field when the field is parallel to hard plane 1 (hard plane 2). It is evident that the spectral weights associated with GS1 and GS2 (i.e., the areas under the resonances) are roughly equivalent, which is consistent with the 50:50 ratio of Δ and Λ isomers. It is also notable

that the hard-plane peaks are considerably sharper for complex **2** than for complex **1** (see Figure 14); even though the data were obtained at different frequencies, the linewidths should be frequency- and field-independent. This finding is consistent with HFEPR studies of many other SMMs, which have suggested that a major contribution to the D-strain comes from disordered solvate molecules.[57–62] In the present case, we note that crystals of **2** do not contain any solvate molecules, whereas crystals of **1** do.

An interesting point to note from Figure 19 is the emergence of excited-state intensity between GS1 and GS2, represented in particular by the two peaks labeled ES1 and ES2 in the top panel of the figure. Each of these two peaks, which have approximately equal intensities, represents a transition from the first excited state ($m_S = -4$) of the corresponding isomer. However, the appearance of these peaks between GS1 and GS2 implies that the first excited-state transition associated with hard plane 1 (ES1) occurs at a higher field than the ground-state transition (GS1). Nevertheless, the field was not aligned within the hard plane for this isomer for the situation displayed in the top panel of Figure 19 (likewise for hard plane 2 in the bottom panel). Indeed, simulations (not shown) indicate that the order of these peaks does in fact reverse for this frequency (94.8 GHz) once the field is tilted significantly (>15°) away from the hard plane, thus confirming the behavior seen in the experiment. Finally, we note that clusters of double-quantum transitions ($\Delta m_S = \pm 2$) are clearly visible at magnetic field strengths below 3 T in Figure 19. Such peaks are often seen in hard-plane measurements, particularly in parallel EPR mode, where the microwave (ac) and dc magnetic fields have parallel components.[63] Thus, the intensities of the $\Delta m_S = \pm 2$ transitions relative to the standard peaks ($\Delta m_S = \pm 1$) tend to depend sensitively on field orientation, as can clearly be seen from comparisons between the upper and lower panels in Figure 19. We point out that these additional peaks greatly complicated our analysis of the frequency-dependent spectra, which is described below.

As with complex **1**, frequency-dependence studies were performed on complex **2** between 50 and 150 GHz at 7 K, with the field (a) as close as possible to one of the two easy axes and (b) precisely aligned in hard plane 2 (see the upper panel of Figure 19); the positions of the EPR peaks seen for these two orientations are plotted in panels a and b, respectively, of Figure 20. Again, the solid curves represent the best simulations of the data obtained via exact diagonalization of eq 6. Before the presentation of the optimum ZFS parameters, some details of our procedure should be discussed. The angle-dependence studies were used to orient the field reasonably close to the easy axis (36° away from the c axis) of one of the species in order to ensure that the strongest peaks would be seen at the lowest fields. As Figure

(61) Amigo, R.; del Barco, E.; Casas, L.; Molins, E.; Tejada, J.; Rutel, I. B.; Mommouton, B.; Dalal, N.; Brooks, J. *Phys. Rev. B* **2002**, *65*, 172403.
(62) Mukhin, A. A.; Travkin, V. D.; Zvezdin, A. K.; Lebedev, S. P.; Caneschi, A.; Gatteschi, D. *Europhys. Lett.* **1998**, *44*, 778–782.
(63) Abragam, A.; Bleaney, B. *Electron Paramagnetic Resonance of Transition Ions*; Dover: New York, 1986.
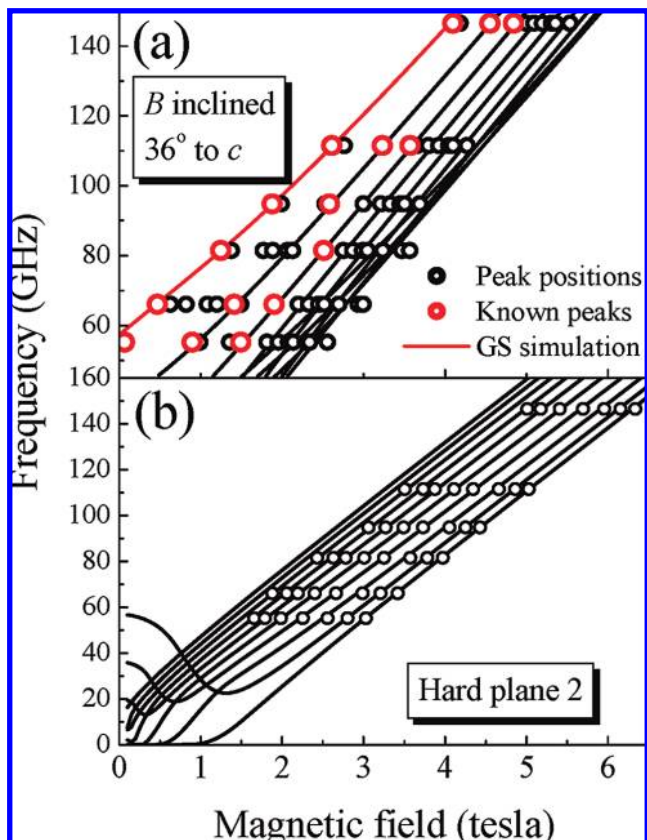
Figure 20. Frequency-dependent HFEPR peak positions for complex **2** between 50 and 150 GHz with the field (a) as close as possible to one of the two easy axes (36° away from the *c* axis) and (b) precisely aligned with hard plane 2. The solid curves represent the best simulations of the data using parameter values obtained from exact diagonalization of the Hamiltonian (eq 6). Red circles represent data points used to constrain the values of the axial ZFS parameters D and B_4^0 (see the text for parameter values used).

20a shows, many other peaks from the second species contaminate the data (moreso at some frequencies than others). Nevertheless, at each frequency we could clearly identify the first two or three of the stronger easy-axis peaks, which have been emphasized in red in the figure. These peaks were used initially to constrain the values of the axial ZFS parameters D and B_4^0, which fix the horizontal spacings of the solid curves; use of just three peaks provided reasonable constraints on these two parameters. Two additional adjustable parameters, g_z and the field orientation, constrain the slopes and curvatures of the solid curves. Best agreement was again obtained for $S = 5$, with optimum axial ZFS parameter values of $D = -0.17$ cm^{-1}, $B_4^0 = -6.68 \times 10^{-5}$ cm^{-1}, and $g_z = 1.98$.

Next we turn to the hard plane 2 data (Figure 20b). A representative spectrum obtained at 81.5 GHz and 7 K is shown in Figure 21 in order to illustrate the problem associated with assigning peaks to the two species. Nevertheless, it was possible to make these assignments by comparing frequency and temperature dependence data. The short upward-pointing arrows in Figure 21 indicate the positions of peaks that we associated with hard plane 2; some of the peaks have been labeled according to the scheme adopted in Figure 19, including GS1 and ES1 corresponding to the other species. The peak positions for hard plane 2 obtained
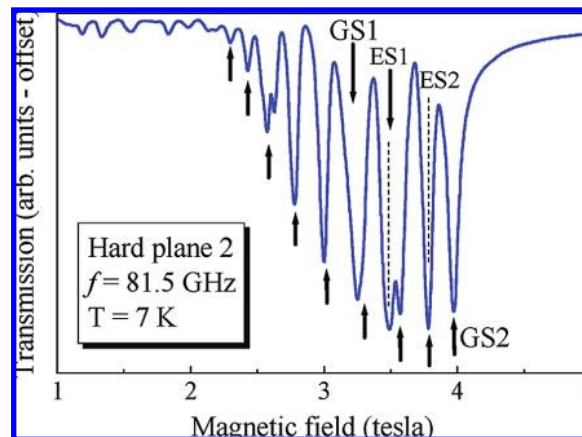
Figure 21. Representative spectrum of hard plane 2 for complex **2** at 81.5 GHz and 7 K. The upward-pointing arrows indicate the peaks assigned to hard plane 2. Peaks for both isomers are labeled according to the scheme described in Figure 19.

at several frequencies are plotted in Figure 20b. In addition to their dependence on the axial parameters D and B_4^0, hard-plane HFEPR spectra are also highly sensitive to transverse interactions.[64] In fact, we found that it was impossible to obtain simultaneous agreement between the data in panels a and b of Figure 20 using only axial ZFS parameters. Therefore, as previously noted, it became necessary to consider transverse anisotropies. Because the orientation of the field within hard plane 2 was not known, it was impossible to obtain precise values for these parameters. Nevertheless, the data do provide valuable insights into the nature of the transverse anisotropy. Surprisingly, we found that good agreement with the data in Figure 20b could not be obtained using only a rhombic E parameter, suggesting the importance of higher-order anisotropies. The simulated curves were generated using the following rhombic parameter values (in addition to the previously obtained axial ones): $E = 6.68 \times 10^{-3}$ cm^{-1}, $B_4^2 = -1.00 \times 10^{-4}$ cm^{-1}, and $g_x = g_y = 1.95$. We stress that while these parameters give reasonable agreement with the data, there could be many other equally good parameter sets involving, for example, terms such as B_4^3, B_4^4, B_6^3, etc. The available data do not provide sufficient constraints to distinguish between these different parameter sets. The main point of these studies was to demonstrate that, in contrast to the other complexes, complex **2** possesses significant transverse anisotropy and that this is the reason for the faster tunneling in **2**.

Concluding Remarks

In summary, we have reported the structure and magnetic properties of four new integer-spin Mn$^{III}_3$Ni^{II} cubane complexes, with **1**, **3**, and **4** exhibiting C_3 molecular symmetry and **2** possessing C_1 symmetry. These complexes exhibit a close structural resemblance to the well-studied half-integer-spin $S = {}^9/_2$ Mn$^{III}_3$Mn^{IV} cubane family. Detailed magnetic susceptibility studies on complexes **1**−**4** indicated ferromagnetic Mn^{III}−Mn^{III} exchange interactions and antiferromag-

(64) del Barco, E.; Kent, A. D.; Hill, S.; North, J. M.; Dalal, N. S.; Rumberger, E. M.; Hendrickson, D. N.; Chakov, N.; Christou, G. *J. Low Temp. Phys.* **2005**, *140*, 119–174.

netic $Mn^{III}-Ni^{II}$ exchange interactions, resulting in well-isolated $S = 5$ spin ground states. Oriented single-crystal HFEPR studies confirmed the spin ground states and established negative D values for complexes **1** and **2**. Single-crystal micro-SQUID hysteresis measurements confirmed that these complexes function as SMMs exhibiting fast QTM, with the low-symmetry complex **2** exhibiting the fastest rate of QTM. These observations parallel results obtained for related $Mn^{III}_3Mn^{IV}$ examples, where complexes with rhombic ZFS ($E \neq 0$) exhibited QTM rates that were larger that those of higher-symmetry complexes. Additionally, the large QTM rates for complexes **1**−**3** highlight the importance of spin-parity effects in SMMs, as these non-Kramers-degenerate SMMs exhibit significantly smaller coercivities than related examples in the $S = {}^9/_2$ Mn_4 cubane family.

Supporting Information Available: ORTEP diagrams for complexes **3** and **4** (Figures S1 and S2), stereo views of the crystal packing for complexes **1** and **4** (Figures S3 and S4), temperature-dependent magnetic susceptibility and multifield magnetization data for complexes **3** and **4** (Figures S5 and S6), ac susceptibility data for complexes **2** and **3** (Figures S7 and S8), sweep-rate-dependent magnetization hysteresis loops for complexes **1**−**3** (Figures S9–S11), temperature-dependent hysteresis loops for $[Mn_4O_3Cl(O_2CCH_3)_3(dbm)_3]_2$ and $[Mn_4O_3(O_2CPh)_4(dbm)_3]$ (Figures S12 and S13), angle-dependent HFEPR spectra for complexes **1** and **2** (Figures S14 and S15), and BVS results for complexes **1**, **3**, and **4** (Table S1). This material is available free of charge via the Internet at http://pubs.acs.org.

IC702241M